

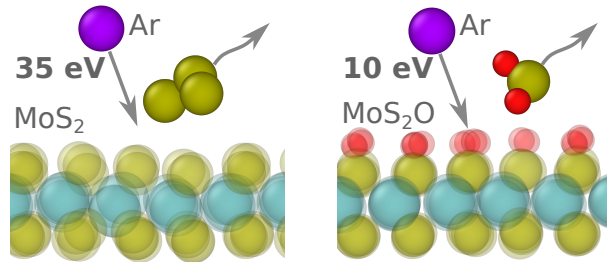
# Transition Metal Dichalcogenide $\text{MoS}_2$ : oxygen and fluorine functionalization for selective plasma processing

Yury Polyachenko,<sup>\*,†,‡</sup> Yuri Barsukov,<sup>†</sup> Shoaib Khalid,<sup>†</sup> and Igor Kaganovich<sup>\*,†</sup>

<sup>†</sup>*Princeton Plasma Physics Laboratory, Princeton, NJ 08540, USA*

<sup>‡</sup>*Department of Chemistry, Princeton University, Princeton, NJ 08544, USA*

E-mail: polyachenkoya@princeton.edu; ikaganov@pppl.gov



## Abstract

Low-temperature plasma processing is a promising technique for tailoring the properties of transition metal dichalcogenides (TMDs) because it allows for precise control of radical and ion energies and fluxes. For chalcogen substitution, a key challenge is to identify the ion energy window that enables selective chalcogen removal while preserving the metal lattice. Using ab-initio molecular dynamics (AIMD), we demonstrate that oxygen and fluorine functionalization through thermal chemisorption significantly lowers the sputtering energy threshold ( $E_{\text{sputt}}$ ) of  $\text{MoS}_2$  from  $\sim 35$  eV to  $\sim 10$  eV. In addition, we find that a non-orthogonal impact angle  $\sim 30^\circ$  reduces the sputtering

energy threshold, while cryogenic-range TMD temperatures may increase. To explain the observed trends, a multi-step sputtering mechanism is proposed. Our results show that oxygen/fluorine functionalization, impact angle, and material temperature are key control parameters for selective, damage-free chalcogen removal in TMD processing.

Plasma processing offers a powerful technique for tailoring material structure and properties.<sup>1</sup> Plasma processing has been widely applied to two-dimensional (2D) materials, including graphene<sup>2–4</sup> and transition metal dichalcogenides (TMDs).<sup>5–11</sup> For TMD processing, ion bombardment underpins a variety of processing steps such as etching, cleaning, and doping<sup>12</sup> where selective removal of targeted atoms is required while preserving the lattice structure. Among TMDs, monolayer MoS<sub>2</sub> in its 2H phase stands out as a particularly promising candidate owing to its direct band gap, comparable to silicon, but at a much smaller thickness. A critical factor in plasma processing of MoS<sub>2</sub> is identifying the ion energy window that enables selective chalcogen removal while preserving the metal lattice.

Pristine MoS<sub>2</sub> has been widely studied through both experimental and theoretical approaches: precise ionic bombardment,<sup>13–19</sup> excitations,<sup>20–26</sup> multi-charged ions,<sup>27–30</sup> ion neutralization,<sup>31–33</sup> substrate effects,<sup>34–36</sup> strain.<sup>37–40</sup> Experiments have shown that Ar+ ions with kinetic energies of approximately 50 eV are sufficient to generate sulfur vacancies (S vacancies), while energies near 100 eV are required to remove Mo atoms and ultimately etch the entire layer in MoS<sub>2</sub>.<sup>13</sup> This establishes a baseline energy window for plasma processing. However, modern techniques are capable of creating ions with temperature as low as  $T_i \sim 1$  eV and also applying a bias of  $\sim 10\text{--}20$  eV.<sup>41,42</sup> This allows controlling ion energies of 10 – 20 eV to within  $\pm 1$  eV. Therefore, these plasmas can be utilized for creating an ion flux with precisely controlled energies. In this work, we calculated the sputtering threshold energy,  $E_{sputt}$ , of MoS<sub>2</sub> with a high accuracy and proposed a novel strategy to reduce this threshold by functionalizing the TMD surface with oxygen or fluorine. Based on ab-initio

molecular dynamics (AIMD) simulations, we developed a sputtering mechanism that explains the observed results, including a prediction of temperature dependence of  $E_{sputt}$  for oxygen-functionalized MoS<sub>2</sub>.

Previous theoretical studies have estimated that to eject a S atom from MoS<sub>2</sub>, approximately 7 eV energy directed exactly outward from the material needs to be transferred to the sulfur atom.<sup>20,43</sup> This value decreases to about 4–6 eV when considering various valence electrons' excitations,<sup>25</sup> and can be as low as 2.2 eV in the presence of multiple excitations of core electrons, i.e. excitations of core electrons. Electron scattering experiments have inferred an effective sulfur desorption energy of approximately 1.5 eV,<sup>21</sup> suggesting that incident electrons generate multiple deep excitations while transferring momentum to the S atom. Low-energy plasma processing is generally conducted with ion energies not exceeding approximately 100 eV.<sup>12</sup> Under these conditions, the generation of deep excitations is unlikely, since the sulfur 2p peaks in XPS spectra of MoS<sub>2</sub>, corresponding to core excitation energies, appear above 150 eV.<sup>44</sup> Moreover, coupling between electronic and ionic motion is inefficient due to their large mass disparity, which makes fast energy transfer to electrons infeasible and gives the ion time to lose its energy in multiple collisions even further. Therefore, we estimate that the lower bound of the sulfur escape energy threshold is  $E_{escape} = 6\text{--}7$  eV.

During TMD-ion collisions, the energy  $E_{escape}$  is what needs to be transferred to the impacted S atom. This transferred energy is smaller than the energy of the incoming projectile  $E_{hit}$  due to the mass ratio  $m_S/m_I \neq 1$  between the impacted S atom and the ion. Therefore, the lower bound for the sputtering projectile energy  $E_{hit}$  is bigger than the escape energy by the by the following factor:

$$E_{hit} = E_{escape} \cdot \left( \frac{\sqrt{m_S/m_I} + \sqrt{m_I/m_S}}{2} \right)^2. \quad (1)$$

However, the collisions are not binary and involve other atoms. Thus, the energy transferred from ion to sulfur atoms can be shared with neighboring molybdenum or other sulfur

atoms so the threshold energy for removal can be higher.

Earlier molecular dynamics simulations on 2D materials have demonstrated that when ion energies exceed 100 eV, the sputtering yield is mainly controlled by secondary collisions involving atoms that are reflected or knocked out from the supporting substrate.<sup>35</sup> However, at lower energies close to the damage threshold (around 10 eV), the sputtering process is expected to be substantially different. In so-called "chemically enhanced physical sputtering," ejecting more chemically stable reaction products rather than individual atoms often reduces the minimum energy required for sputtering.<sup>45</sup> When an ion collides with the top sulfur atom, a sulfur atom initiates cascade of intermediate collisions that can affect TMD lattice and even substrate. Careful consideration needs to be given to these intermediate collisions so that TMD lattice is restored after the collision and is not damaged.

In this research, we propose a two-step chemically-enhanced physical sputtering mechanism that minimizes the sputtering threshold energy  $E_{sputt}$  of MoS<sub>2</sub> functionalized by oxygen or fluorine:

1. The Ar impact induces atomic rearrangements that facilitate the formation of (meta)stable gas-phase species such as SO<sub>2</sub>, SF<sub>4</sub>.
2. Under the above condition, efficient momentum transfer from the incoming Ar to the ejected molecular species is achieved by optimizing the number and directions of intermediate collisions that lead to desorption of these products.

The simulation setup for collisions of the incoming Ar with monolayer MoS<sub>2</sub> is shown in Fig. 1.

In this paper, we show that oxygen or fluorine functionalization reduces the sputtering threshold energy  $E_{sputt}$  in MoS<sub>2</sub>, as illustrated in Fig. 2. This phenomenon is explained by the observation that small (meta)stable molecular fragments, such as SO<sub>2</sub> and SF<sub>4</sub>, can form more easily from a few TMD atoms actively involved in a low-energy Ar impact, compared to ejection of pure sulfur atoms or clusters (S<sub>2</sub>, S<sub>6</sub>, or S<sub>8</sub>). The enhanced formation of

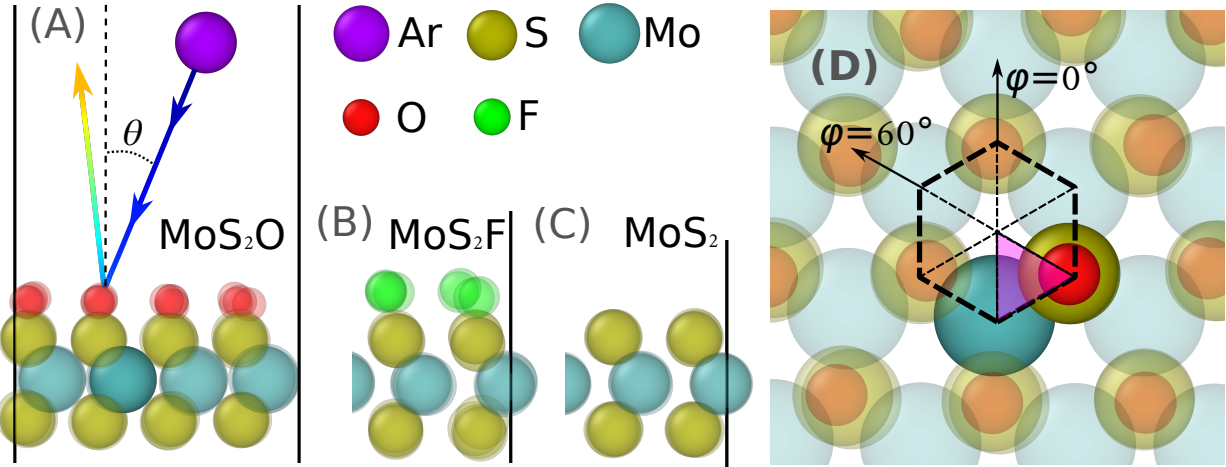


Figure 1: Simulation setup schematic. (A): Side view of the full MoS<sub>2</sub>O equilibrated supercell (4x4) initial state. Ar atom's trajectory is shown by a rainbow line with color representing time from blue to red. (B,C): Representative parts of the MoS<sub>2</sub>F and MoS<sub>2</sub> initial equilibrated states (side view), respectively. Irregularity of fluorine atoms' positions is discussed in the main text. (D): Top view of MoS<sub>2</sub>O. The purple shade triangle shows the minimal set of hit-points that represents all other points by symmetry. The in-plane far-field approach angle,  $\varphi$ , shows its origin  $\varphi = 0^\circ$  and its positive direction  $\varphi = 60^\circ$ . The hit angle remains very close to the initial far-approach angle in cases considered in this study.

these O or F containing fragments can be attributed to O/F high electronegativity, which stabilizes intermediate fragments relative to the rest of the material and facilitates their ejection under lower-energy impacts. These findings suggest that selective functionalization provides a practical route to control the sputtering behavior of TMDs at energies near the damage threshold.

As a preliminary step, we examined the feasibility of O and F adsorption on MoS<sub>2</sub> before analyzing the impacts of O and F covered surfaces. It is well known that oxygen exhibits strong reactivity with TMDs.<sup>46–57</sup> For example, even molecular O<sub>2</sub> has been shown to fill S vacancies in MoS<sub>2</sub> with an activation barrier of approximately 1.05 eV.<sup>47</sup> Previous calculations have further indicated that O<sub>2</sub> can dissociate into atomic oxygen, and, subsequently, adsorb onto MoS<sub>2</sub>, with a total barrier of about 1.6 eV.<sup>53</sup> Isolated atomic oxygen was also reported to adsorb on MoS<sub>2</sub> with a binding energy of 0.88–1.12 eV, depending on the surface coverage.<sup>53</sup> Our calculated adsorption energy for O on MoS<sub>2</sub> is in close agreement with

the previous results, as shown in the Figure 8B of the supplementary information (SI).<sup>58</sup> Furthermore, we performed meta-dynamics calculations to verify that our conclusions based on the potential energy surfaces (PES) qualitatively hold for the corresponding free-energy surfaces (FES) as shown in Figure 8D and 8E.

Oxygen has been experimentally shown to play a significant role in the thermal etching of TMDs, initiating around 345°C.<sup>54</sup> Under ambient conditions, ~month-long exposure to molecular O<sub>2</sub> also induces sulfur vacancies.<sup>55</sup> In both cases, the formation of stable gas-phase species such as SO<sub>2</sub> has been proposed as a key step in oxygen-assisted etching.

Building on these observations, we consider how thermally adsorbed oxygen and fluorine can similarly facilitate chalcogen removal in TMDs. We propose that such functionalization could extend the Ar ion energy window for plasma processing and enhance the selective removal of chalcogen atoms while preserving the underlying metal lattice.

We first investigate impacts orthogonal to the material plane ( $\theta = 0$ , see Figure 1A). Figure 2 shows the probabilities of sulfur ejection for pristine and functionalized MoS<sub>2</sub>. Atomic oxygen functionalization decreases  $E_{sputt}$  from  $\sim (31 \pm 1)$  eV to  $\sim (14.0 \pm 1)$  eV. Atomic fluorine is even more effective with  $E_{sputt} \sim (9.5 \pm 0.5)$  eV. The error bars represent the spacing of the energy grid used to determine the sputtering threshold, rather than a measure of statistical uncertainty. The precise threshold values can change depending on the specific approximations used in MD simulations, such as the selected functional or pseudopotential. For this reason, we did not further refine the energy grid. However, the qualitative relative effect of the substantial reduction in  $E_{sputt}$  is insensitive to the specific DFT implementation, as it arises from clear physical mechanisms discussed below.

These results suggest that O and F pre-functionalization can effectively expand the ionic energy window for plasma processing, allowing selective chalcogen removal at lower projectile energies, while minimizing damage to the underlying metal scaffold.

A qualitative understanding of why the threshold drops so significantly can be obtained by examining ejection events that are representative of MoS<sub>2</sub>O and MoS<sub>2</sub>F, as shown in

Back-sputtering at functionalizations ( $\bullet$ /O/F); Orthogonal  $\perp$  hit

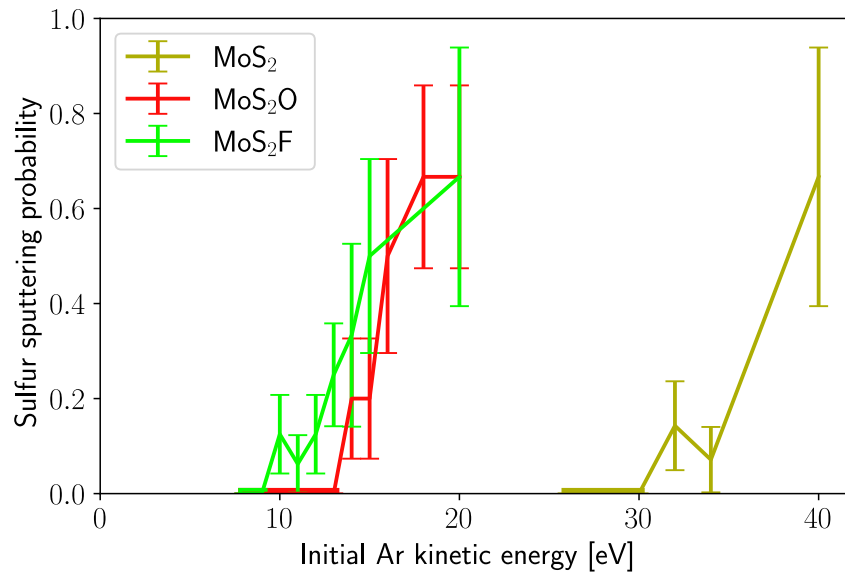


Figure 2: Probability to eject sulfur from pristine and functionalized MoS<sub>2</sub> back into the semi-space the impact came from. Functionalization with O and F substantially lowers the sputtering threshold energy, indicating enhanced chalcogen removal efficiency at reduced Ar energies. For each of 3 TMDs, the impact point was optimized to minimize  $E_{sputt}$  (details on Figure 9. Materials were equilibrated at 116K.

Figures 3 and 6.

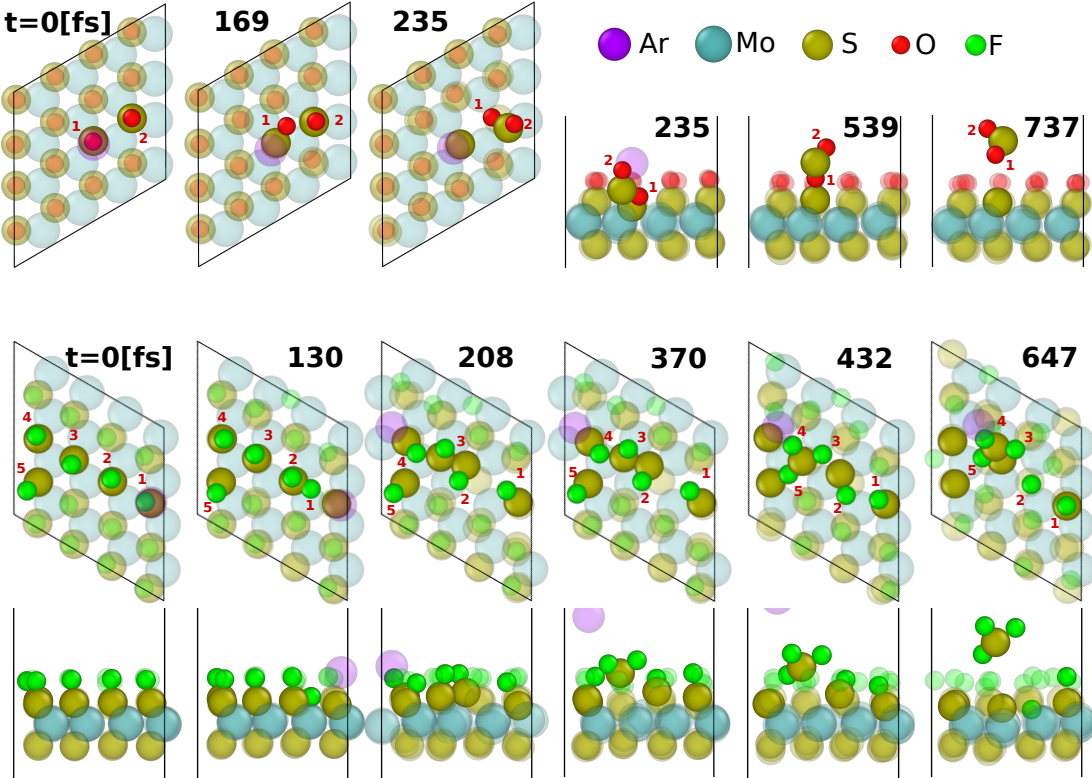


Figure 3: (Top): A typical orthogonal Ar collision with  $\text{MoS}_2\text{O}$ . Opaque atoms are those that ultimately play a major role in the collision. Gray numbers are timestamps in [fs]. The sputtering mechanism of  $\text{MoS}_2\text{O}$  that realizes at the lowest required projectile energy involves an O atom being pushed in the direction of the nearest S atom that already has another O bound to it, allowing them to combine and form  $\text{SO}_2$ , which then escapes. Small red numbers innumerate O atoms to help following them during collisions. A collision at an angle is shown in video V1. (Middle and Bottom): A typical orthogonal Ar collision with  $\text{MoS}_2\text{F}$ . Side and top views are both provided to illustrate more complex atom movements during the collisions. Small red numbers innumerate F atoms to help following them during collisions. Both materials were equilibrated at 116 K, both impacts were with 15 eV.

A typical collision that result in sulfur sputtering from a O- or F- functionalized  $\text{MoS}_2$  involves formation of (meta)stable products (such as  $\text{SO}_2$  or  $\text{SF}_4$ ) that later escape. This is different from pristine  $\text{MoS}_2$  sputtering (details are provided in Figure 6) that first mechanically breaks bonds of S atoms that later may assemble into  $\text{S}_n$  cluster products. Accordingly, we ascribe the substantial variation in sputtering energy thresholds to the distinct sputtering mechanisms involved.

A noticeable difference in typical collision events between  $\text{MoS}_2\text{O}$  and  $\text{MoS}_2\text{F}$  is attributed

to the differences in equilibrium positions of absorbed O and F atoms on the TMD surface, shown on Figure 3 (at  $t = 0$ ). More details are discussed in the SI.<sup>58</sup>

The MoS<sub>2</sub>O structure keeps all symmetries of MoS<sub>2</sub> and oxygen atoms are absorbed directly above the sulfur atoms, see Figure 3 ( $t = 0$ ) and Figure 10. In contrast, the MoS<sub>2</sub>F has a more disordered F layer (see Figure 3 at  $t = 0$  and Figure 11). This leads to more chaotic collision dynamics. This is indicated by 5 F atoms significantly participating in the MoS<sub>2</sub>F impact, as opposed to only 2 O atoms for the MoS<sub>2</sub>O impact. Sputtering probabilities as a function of the ejected species for conditions of Figure 2 is shown in Figure 7. It suggests that sputtering products from MoS<sub>2</sub>F are more varied than that from MoS<sub>2</sub>O, which further indicates more disorder in the MoS<sub>2</sub>F case. A similar diversity of SF<sub>n</sub> products was reported before for F<sub>2</sub> plasma.<sup>59</sup>

The observed difference in MoS<sub>2</sub>O and MoS<sub>2</sub>F ground states may be utilized for high-specificity etching due to the following: Because the MoS<sub>2</sub>O preserves the well structured MoS<sub>2</sub> lattice, collision results depend strongly on Ar incident angle. Correspondingly, a strong angular dependence in sputtering threshold was found for MoS<sub>2</sub>O and MoS<sub>2</sub> as shown in Figure 4.

The threshold decreases significantly and non-monotonically with increasing impact angle, reaching about  $(7.5 \pm 0.5)\text{eV} = E_{\text{sputt}}(\theta = 30^\circ) \approx 0.54 \cdot E_{\text{sputt}}(\theta = 0^\circ)$  for the MoS<sub>2</sub>O. The value  $E_{\text{sputt}}(\theta = 45^\circ)$  (not shown on the plot) is  $> 14$  eV, so  $\theta \approx 30^\circ$  is optimal for sputtering MoS<sub>2</sub>O. A similar decrease by  $\sim 6\text{-}7$  eV is seen for pristine MoS<sub>2</sub>, which also has a clear periodic structure before the impact.

These three presented TMD cases demonstrate a correlation between the degree of order in a system's ground state and its sensitivity to the angle of projectile impacts. Specifically, sufficiently disordered systems such as MoS<sub>2</sub>F lose their sensitivity to impact direction.

To solidify our understanding of the proposed sputtering mechanisms, we formulate a simple theory that predicts the dependence of the sputtering threshold  $E_{\text{sputt}}$  on the TMD temperature  $T$ . The theory does not require MD simulations at different temperatures, but

Back-sputtering Sulfur with suppressed fluctuations (T=1K)

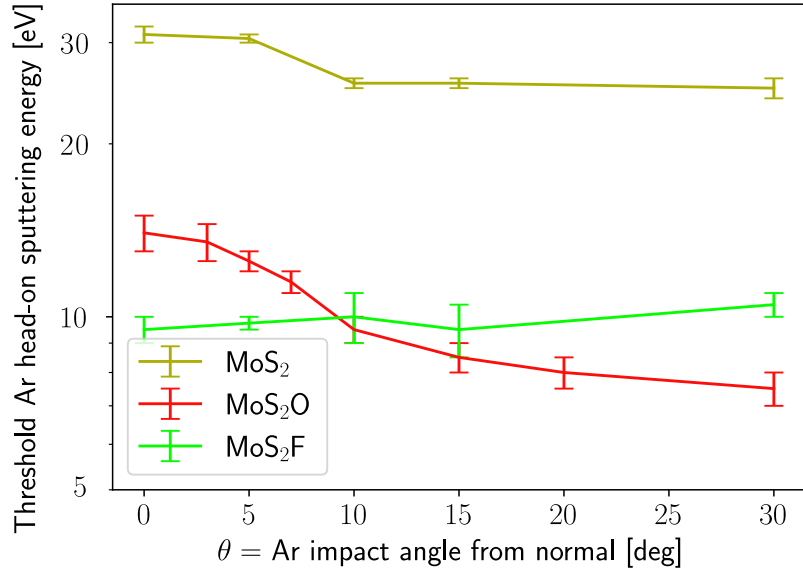


Figure 4: Angular dependence of the sputtering threshold energy  $E_{sputt}$  for MoS<sub>2</sub> (dark yellow), MoS<sub>2</sub>F (light green) and MoS<sub>2</sub>O (red) for head-on impacts. Thermal fluctuations of target S/F/O atoms in the system are suppressed by formally setting  $T = 1\text{K}$ . Each curve is obtained after optimizing the impact point and the in-plane angle  $\varphi$  to minimize  $E_{sputt}$ , as shown on Figure 15 for MoS<sub>2</sub>O. Simulations at  $\theta = 45^\circ$  were done for MoS<sub>2</sub> and MoS<sub>2</sub>O and they showed  $E_{MoS_2}(45^\circ) > 35\text{ eV}$  and  $E_{MoS_2O}(45^\circ) > 14\text{ eV}$ . Error bars reflect the step of the energy grid used to pin down the threshold.

uses only the temperature-independent curve  $E_{sputt}(\theta)$  from 4 and simple collision models (see SI). We show below that such a simple and parameter-free theory is well correlated with MD simulation results, suggesting the proposed simple mechanisms indeed take place.

The proposed theory is based on connecting the angular dependence  $E_{sputt}(\theta)$  and thermal fluctuations of target atoms, which cause an unavoidable spread in deflection angles. Because the magnitude of thermal fluctuations of target O/F atoms (about 0.15 Å, Figure 14) in the material is comparable to the distances at which Ar interacts strongly with the O/F atoms (i.e., hard-core repulsion interaction distance, about 1 Å, see Figure 14), a certain range of deflection angles,  $\theta_T$ , often realizes due to thermal fluctuations. On the other hand, each impact Ar energy  $E_{Ar\perp}$  has a threshold angle  $\theta_{thr}(E_{Ar\perp})$  so that impacts a larger angles  $\theta > \theta_{thr}(E_{Ar\perp})$  result in sputtering. This means that if the thermal spread of deflection

angles  $\theta_T$  covers  $\theta_{thr}$  for a given temperature, i.e.  $\theta_T(E_{Ar\perp}) > \theta_{thr}(E_{At\perp})$ , then deflection angles sufficient for sputtering at the given  $E_{Ar\perp}$  will be realized often, so sputtering will be often. This is quantitatively explained in the SI in Figure 13. Quantification of this logic is given in SI,<sup>58</sup> and it yields the dashed line on Figure 5.

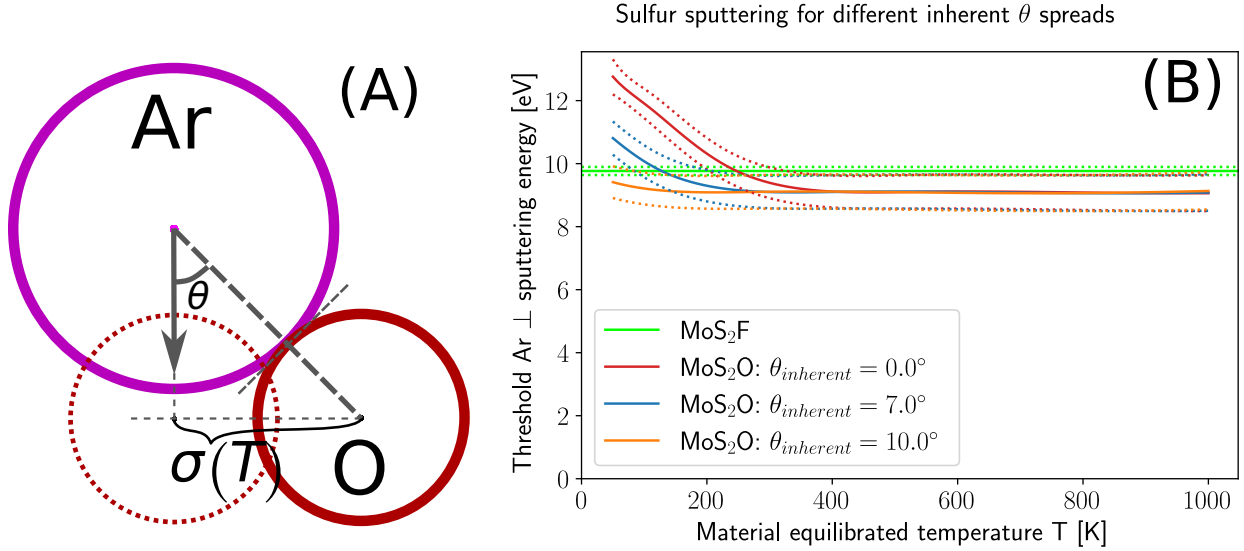


Figure 5: (A): A schematic showing an Ar impacting an O atom. The Ar velocity is directed exactly at the O equilibrium position, which was shown to be the most damage-susceptible point of MoS<sub>2</sub>O in Figure 9. However, the impact is not head-on due to a thermal fluctuation of magnitude  $\sigma(T)$  of the O atom. (B): Red, blue and yellow: Our predictions for  $E_{\perp,sputt}(T)$  of MoS<sub>2</sub>O for inherent  $\theta$ -spreads of the incoming Ar of 0°, 7°, and 10° respectively. Green: the  $T$ -independent  $E_{sputt}$  of MoS<sub>2</sub>F. No fitting parameters were used in the theory, except for data interpolation of  $E_{Ar-O}(\theta)$  on Figure 4. Curves for no inherent spread ( $\theta_{inherent} = 0$ ) show a good match to MD simulation results (Figure 17).

Notably, this is a parameter-free theory in a sense that no fitting to AIMD  $E_{sputt}(T)$  was done to obtain red dashed theory line in Figure 17. Still, the predicted behavior is confirmed in AIMD simulations. It suggests the proposed sputtering mechanism and the theory that follows from it are reasonable and consistent approximations that provide insights into atomistic mechanisms of sputtering of MoS<sub>2</sub> and its functionalized modifications. Therefore, the proposed sputtering picture can inform TMD simulations at the continuum level and potentially explain the nonlinearities associated with the involving oxygen.<sup>60</sup>

Our analysis shows how functionalization of MoS<sub>2</sub> with O or F can significantly lower

the sputtering energy threshold from  $\sim 30$  eV down to  $\sim 10$  eV, as shown in Figure 2. Such functionalization may be used for TMD processing with minimal damage to the metal scaffold. Additionally, this type of functionalization enables spatial control over the etching process, which can be realized by selectively depositing oxygen or fluorine in accordance with a mask. Employing partial coverage with oxygen/ fluorine can allow accurate control over the creation of sulfur vacancies by selectively sputtering a defined fraction of surface atoms that have been functionalized with oxygen/ fluorine, and this approach is relatively insensitive to the exact plasma exposure time.

More specifically,  $\text{MoS}_2$  and  $\text{MoS}_2\text{O}$  exhibit ranges of possible threshold energies: 32 – 24 eV and 14 – 7.5 eV, respectively—which depend on the impact angle (Figure 4). However, achieving the threshold energies of  $\sim (32 \pm 1)$  eV for  $\text{MoS}_2$  and  $\sim (14 \pm 1)$  eV for  $\text{MoS}_2\text{O}$  under strictly normal Ar incidence is likely challenging under realistic plasma conditions (Figure 5,  $\theta_{inherent} > 0$ ), where projectiles exhibit an angular spread. In practice, the effective threshold values will be lower because temperature effects disrupt perfectly orthogonal impacts. First, plasma ions has transverse temperature at least of  $\sim 0.1$  eV, which creates a spread in impact angles  $\sim 5^\circ$  even under low-pressure conditions.<sup>61</sup> Secondly, even if some ions impinge on the TMD surface in a truly orthogonal direction and hit O atoms, the O atoms deflect with the an angular spread  $\theta_T$  (Figure 5,  $\theta_{inherent} = 0$ ). This spread,  $\theta_T$ , is determined by the TMD temperature, because thermal fluctuations of the target O atoms grow with increasing temperature, roughly following a  $\sim \sqrt{T}$  scaling. Therefore, the thresholds observed in experiments are more likely to be closer to  $\approx (26 \pm 2)$  eV for  $\text{MoS}_2$  and  $\sim (9 \pm 1)$  eV for  $\text{MoS}_2\text{O}$ . By tightly restricting the Ar incidence angle to within a spread of  $< 5^\circ$  and minimizing thermal fluctuations by cooling the TMD to cryogenic temperatures of approximately  $(-200$  to  $-50)^\circ\text{C}$ , it may be possible to increase the threshold closer to  $\sim (31 \pm 2)$  eV for  $\text{MoS}_2$  and  $\sim (13 \pm 1)$  eV for  $\text{MoS}_2\text{O}$ . To observe the proposed temperature sensitivity, one can also use narrow beams with a very small angular divergence.

One should also keep in mind the limitations of the reported findings. First, the precise

numerical values of the reported energy thresholds can depend on the specific details employed in the DFT calculations. However, the key conclusions that sputtering is substantially enhanced by oxygen/fluorine functionalization (and also increased with the impact angle) follow from straightforward physical arguments, indicating that they should remain valid independent of the specific DFT implementation. Second, the proposed sputtering mechanism where products such as  $\text{SO}_2$  and  $\text{SF}_n$  are formed and then desorb, assumes a high surface coverage of oxygen and fluorine. At low coverage, however, different mechanisms are expected, since the formation of  $\text{SO}_2$  and  $\text{SF}_n$  under these conditions is unlikely. Furthermore, a realistic ion angular spread of about  $5\text{--}10^\circ$ <sup>61</sup> would decrease the temperature sensitivity, as shown in Figure 5. More MD simulations may help to quantify such effects. Finally, cleaning the functionalizing O/F atoms after achieving the desired processing effect requires additional steps. There are reported approaches to address that.<sup>52</sup>

## Acknowledgement

This material is based upon work supported by the U.S. Department of Energy, Office of Science, Fusion Energy Sciences and Basic Energy Sciences, as part of the Extreme Lithography & Materials Innovation Center (ELMIC), a Microelectronics Science Research Center (MSRC), under contract number No. DEAC02-09CH11466. The simulations were carried out at the National Energy Research Scientific Computing Center (NERSC), a U.S. Department of Energy Office of Science User Facility located at Lawrence Berkeley National Laboratory, operated under Contract No. DE-AC02-05CH11231 using NERSC award BES-ERCAP33081/BES-ERCAP32938 and the Stellar, Della, and Tiger clusters at Princeton University. We would like to thank John Mark Martinez, Jack Draney, Louis Hoffenberg, and David Graves for fruitful discussions.

## Supporting Information Available

### Origins of $\text{MoS}_2\text{O}$ vs $\text{MoS}_2\text{F}$ sputtering mechanism differences:

We hypothesize that forming  $\text{SO}_2$  is the key step for  $\text{MoS}_2\text{O}$  sputtering (Figure 3), which will inevitably lead to thermal desorption of  $\text{SO}_2$ . This means that only a single S-O bond needs to be broken by Ar to enable such a sputtering mechanism. Forming products  $\text{SF}_n$ , on the other hand, may not be sufficient for their subsequent thermal desorption because they are much more reactive. Thus, weakening of the Mo-S bonds by F atoms, due to its high electronegativity may be a necessary part of the decrease in the sputtering energy threshold.

A chemical reason for symmetry breaking in  $\text{MoS}_2\text{F}$ , but not in  $\text{MoS}_2\text{O}$  can be rooted in the electronegativity difference between F and O. The more electronegative F can pull more electron density from S. The S-F bond is also longer than S-O ( $d_{bond} \approx 1.9 \text{ \AA}$  vs  $1.4 \text{ \AA}$ , see Figure 8A). This creates a stronger dipole  $\sim d_{bond}q_{bond}$  in each S-F pair. Such dipole formation was reported for  $\text{MoS}_2\text{O}$ .<sup>62</sup> All dipoles are aligned, making them repulsive, and this repulsion is stronger for S-F dipoles. Thus, this may impose sufficient stress on  $\text{MoS}_2$  to break its symmetry.

We note that typical sputtering events reported here occur on the timescale  $< 1 \text{ ps}$ , as shown in Figures 3 and 6. This does not mean sputtering is impossible at lower energies; for example, even thermal sputtering on a timescale of month is feasible.<sup>55</sup> We also observed a multi-step S-vacancy creation process on timescales as long as  $\sim 20 \text{ ps}$  (shown on Figure 12). However, such events exhibit a clear separation of timescales between the product formation and product removal. An Ar impact that is not sufficient for fast ejection of products can still catalyze product formation, with subsequent thermal desorption occurring on a much longer timescale. Since most immediate sputtering events we observed occurred within  $< 1 \text{ ps}$ , we chose 2 ps as the timescale to separate "immediate" sputtering from thermal desorption of

products. Thus, we simulate for 2 ps after the impact and conclude that no sputtering has occurred if the products do not detach from the material within this time.

## Angular sensitivity $\Leftrightarrow$ ground-state order:

Fluorinated MoS<sub>2</sub>, which is less ordered than MoS<sub>2</sub>O even before the impact, shows no systematic variation with increasing impact angle. This indicates that once the symmetry is disrupted, further changes in the direction of incoming projectiles have little additional effect on the sputtering behavior. This is because the main effect of a slight tilt of the impact from the surface normal is to allow the impacted O/F to pass by the S atom directly below it, thereby enabling the O/F to break its bond with S and potentially initiate the formation of sputtering products. Such tilting is necessary for MoS<sub>2</sub>O where O atoms sit directly on top of S atoms, whereas F atoms are already slightly shifted from their underlying S atoms, so small additional tilts do not produce a significant change.

The in-plane angle  $\varphi$  is also shown to be important for MoS<sub>2</sub>O (Figure 15). We found in-plane angles that maximize sputtering to be  $\varphi_{opt}(O) = 30^\circ$  and  $\varphi_{opt}(S) = 0^\circ$ . Fluorine did not show sensitivity to  $\varphi$ . This is consistent with proposed sputtering mechanisms: Pristine MoS<sub>2</sub> is sputtered by physically breaking the bonds of a single S atom, which requires that other in-plane atoms do not obstruct the S atom as it gains maximum displacement, while still preventing it from penetrating too deeply into the material in order to minimize intermediate collisions. This condition is achieved at  $\varphi = 0^\circ$  (see Figure 1D) where the impacted S atom has the largest available in-plane space in the reflection direction. The hit-point at the center of the hexagon (which was found to be optimal for MoS<sub>2</sub>) leads to the projectile energy being distributed approximately equally among three Mo atoms, such that no single Mo atom deviates too far from its equilibrium position and collides with its neighbors. The temporary storage and redistribution of projectile energy in this case is more complex and likely involves several many-body effects. The mechanism for MoS<sub>2</sub>O,

on the other hand, involves the formation of  $\text{SO}_2$ , which subsequently escapes. Impacting an O atom at  $\varphi = 30^\circ$  directs it toward its nearest S neighbor that has another O atom attached(see Figure 1D). Thus,  $\text{SO}_2$  formation is expected to be maximized at  $\varphi = 30^\circ$ , with the hit-point directly on the oxygen. Finally, the insensitivity of  $\text{MoS}_2\text{F}$  to  $\varphi$  again highlights how structural disorder suppresses its directional response.

## Finding the most damage-susceptible hit point:

An analysis similar to Figure 9 was also performed for  $\text{MoS}_2\text{F}$ . It showed that the above-sulfur site is among the most susceptible. Different F atoms are displaced by different amounts from being directly above their S atoms, which means that a head-on collision requires a hit-point slightly offset from the directly above-sulfur position. We speculate that the effect of this shift is negligible, because the directional insensitivity of  $\text{MoS}_2\text{F}$  arises not only from the random strong displacements of the equilibrium positions of the directly impacted F atoms, but also from the surrounding F atoms. These surrounding F atoms will still not be sufficiently ordered even if the initial Ar-F impact is head-on. Analogous tests for  $\text{MoS}_2$  find the most susceptible point to be at the center of the 3Mo-3S hexagon (the Ar position in Figure 6 at  $t=0$ ). We speculate that this is because it is the most effective hit-point for the sputtering mechanism shown in 6. This mechanism is likely the most energy-efficient, as the reversal of the projectile velocity occurs via "reflection" from the Mo layer through approximately equal displacement of three Mo atoms. As a result, the maximum Mo displacement is minimized, reducing Mo-Mo collisions with neighboring atoms and thereby minimizing energy losses.

## Simple theory for $\text{MoS}_2\text{O}$ $E_{sputt}(T)$ :

The qualitative difference in the angular dependence  $E_{sputt}(\theta)$  between  $\text{MoS}_2\text{O}$  and  $\text{MoS}_2\text{F}$  has important implications for their temperature dependence since thermal fluctuations lead

to a finite spread in reflection angles even for orthogonal impacts. This angular spread is non-negligible because the magnitude of thermal fluctuations of O and F atoms in the material plane is comparable to their hard-core repulsion interaction distance with Ar (see Figure 16). This means that even orthogonal impacts will not always result in strictly vertical momentum transfer. Instead, thermal fluctuations of O/F atoms make the collision non-head on, thus introducing a distribution of reflection angles (see SI and Figure 16):

$$\theta_T(E_{Ar\perp}) \approx \arcsin \left( \frac{\sigma_{xy,X}(T)s_N}{r_{Ar-X}(E_{Ar\perp}, \theta_T(E_{Ar\perp}))} \right) \quad (2)$$

where  $\sigma_{xy,X}(T)$  represents the magnitude of thermal fluctuations of X={O,F} in the plane of MoS<sub>2</sub>, (see Fig 14 for its temperature dependence). The scale factor  $s_N = \chi_1.PPF(1 - 1/(N + 1))$  comes from our definition of the sputtering threshold. We have a finite sample of  $N$  impact trials, and we register sputtering if at least one trial results in sputtering. This means that the maximum fluctuation of magnitude  $\sigma$  over all  $N$  trials has the probability of exceeding  $\sigma_N$  equal to the probability of a single fluctuation exceeding  $\sigma$ . Therefore, we use  $\sigma_N = \sigma s_N$  as a characteristic fluctuation size instead of just  $\sigma$ . In a normal case,  $\sigma_{xy}$  would be distributed  $\sim \chi_2 = \sqrt{\chi_2^2}$  due to  $\sqrt{\sigma_x^2 + \sigma_y^2}$ . However, only a narrow direction of  $\phi$  angles is susceptible to damage near the sputtering energy threshold (Figure 15), so only deviations along a single axis are relevant, and the distribution reduces to  $\chi_1$  in our case. Since we require the probability of observing a deviation larger than  $\sigma_N$  at least once in  $N$  trials to be significant, we set  $\chi_1.CDF(\sigma_N/\sigma) = 1 - 1/(N + 1)$ , where  $N + 1$  instead of  $N$  is used to remove singularity at  $N + 1$ . This means that a single fluctuation has a probability  $1/(N + 1)$  of exceeding  $\sigma_N$ . Thus  $\sigma_N = \sigma \cdot \chi_1.CDF^{-1}(1 - 1/(N + 1)) = \sigma \cdot \chi_1.PPF(1 - 1/(N + 1))$ . For large  $N$ , this quantity has a weak dependence of  $\approx \sqrt{2 \ln(N + 1)}$ , therefore the exact number of trials is not substantially important.

The term  $r_{Ar-X}$  denotes the Ar-X interatomic distance, defined as the sum of hard sphere radii that approximate the interacting atoms during the collision. It is determined by how closely the head-on component of the collision energy,  $E_{Ar\perp} \cos^2(\theta)$  brings the atoms

together. Thus, it depends on the impact energy and collision geometry as described below (see SI for details):

$$U_{Ar-X}(r_{Ar-X}) = \frac{E_{Ar\perp} \cos^2 \theta}{1 + m_X/m_{Ar}} \quad (3)$$

where  $U_{Ar-X}$  is the two-atom potential energy surface (PES) between Ar and X. We take its inverse function  $U_{Ar-X}^{-1}$  such that  $r = U_{Ar-X}^{-1}(E)$  is the interatomic distance at which  $U_{Ar-X}(r) = E$ . The factor  $1 + m_X/m_{Ar}$  comes from the center-of-mass frame treatment of collision.

For typical relevant  $(E_{Ar\perp}, T)$  ranges, the in-plane thermal fluctuations are smaller than the collisional radii of the atoms, which results in a narrow spread of the reflection angle  $\theta_T$ . More precisely,  $\sigma_{xy,X}(T) \ll r_{Ar-X}(E_{Ar\perp}, \theta_T(E_{Ar\perp}))$ , which leads to  $\theta_T \ll 1$ . Therefore, we can write  $r_{Ar-X}(E_{Ar\perp}, \theta_T(E_{Ar\perp})) \approx r_{Ar-X}(E_{Ar\perp}, 0) = r_{Ar-X}(E_{Ar\perp})$ . We can also assume a harmonic potential well for small  $\sigma_{xy,X}(T)$ , which leads to  $\sigma(T) = \sigma_0 \sqrt{T/T_0} \propto \sqrt{T}$  where  $\sigma_0 = \sigma_{xy,X}(T_0)$ . The scaling  $\sim \sqrt{T}$  is confirmed in Figure 14. Combining this, we can write an approximate explicit expression

$$\theta_T(E_{Ar\perp}) \approx \arcsin \left( \frac{\sigma_0 s_N}{r_{Ar-X}(E_{Ar\perp})} \sqrt{\frac{T}{T_0}} \right) \approx \frac{\sigma_0 s_N}{r_{Ar-X}(E_{Ar\perp})} \sqrt{\frac{T}{T_0}} \quad (4)$$

Thus, an O or F atom fluctuating at temperature  $T$  and impacted by an Ar atom with orthogonal energy  $E_{Ar\perp}$  can acquire velocities distributed within an angular range of  $\theta \approx 0 \pm \theta_T(E_{Ar\perp})$ .

On the other hand, it is possible to isolate the effect of impact non-normality from thermal noise by bombarding surfaces equilibrated at temperatures low enough that thermal fluctuations are negligible, meaning  $\sigma_{xy}(T) \ll d_{atom} = r_{Ar-X}(E_{sputt,min})$ . The results are shown in Figure 13A. No significant angle dependence is observed for MoS<sub>2</sub>F, as expected from its irregular ground state structure. However, MoS<sub>2</sub>O exhibits a non-linear decrease in  $E_{sputt}(\theta)$ , dropping by  $\sim 40 - 50\%$  at  $\theta \sim 10 - 15^\circ$  before flattening. Although not

shown in the plot, it starts rising at some point  $\theta_{opt}$  between  $30^\circ$  and  $45^\circ$ . The curve  $E_{Ar-X}(\theta < \theta_{opt})$  therefore represents the energy threshold that Ar must have in a head-on, non-normal collision with X to induce ejection of an S atom.

Thus, eq.(2) gives the range of reflection angles that are thermally accessible (purple shade on Figure 13B), while the inverted curve  $E_{Ar-X}(\theta)$  from Figure 4A provides the minimum reflection angles  $\theta_{Ar-X}(E_{head-on})$  required for sputtering (blue shade on Figure 13B). As the angular spread increases with  $T$ , once angles  $\theta > \theta_{Ar-X}(E_1)$  become thermally accessible at a certain temperature  $T_1$ , sputtering with  $E_{head-on} = E_1$  becomes frequent at  $T > T_1$ . See the SI for the derivation of the purple curve in Figure 13B. Solving eq.(5) for X=Oxygen numerically gives the red dashed line in Figure 5.

## 2-body collision model:

To translate the head-on, non-normal energy threshold  $E_{Ar-X}(\theta)$  into a threshold for a non-head-on but normal impact,  $E_{Ar\perp}(\theta)$ , we recall that only a factor of  $\cos^2(\theta)$  of the total energy participates in the collision when the reflection angle is  $\theta$ . This yields  $E_{Ar\perp}(\theta) \cos^2(\theta) = E_{Ar-X}(\theta)$ . This results in a system of two equations with two unknowns  $(\theta_T, E_{Ar\perp})$ :

$$\begin{cases} U_{Ar-X} \left( \frac{\sigma_{xy}(T)}{\sin(\theta_T)} \right) = \frac{E_{Ar\perp} \cos^2(\theta_T)}{1 + m_X/m_{Ar}} \Rightarrow \theta_T(E_{Ar\perp}) \\ E_{Ar\perp} = \frac{E_{Ar-X}(\theta_T(E_{Ar\perp}))}{\cos^2(\theta_T(E_{Ar\perp}))} \Rightarrow E_{Ar\perp}(T) \end{cases} \quad (5)$$

where the first equation describes the spread of reflection angles of the impacted O/F atoms and the second equation relates the normal, non-head-on impact energy (which is often controlled experimentally) to the non-normal head-on energy (which is easier to simulate and is temperature independent to a good approximation).

The two equations correspond to two physical conditions required for sputtering in the proposed mechanism: thermal fluctuations of the impacted O/F should be wide enough to allow the reflection angle spread  $\theta_T$  that includes angles sufficient for sputtering according

to  $E_{Ar-X}(\theta)$ . This breaks down into 2 conditions:

1. At a given temperature  $T$ , normal Ar impact induce a spread of reflection angles  $\theta < \theta_T$ . The purple region in Figure 5A corresponds to such a region for  $T = 300\text{K}$ . There is also a slight dependence on  $E_{Ar\perp}$ , because higher  $E_{Ar\perp}$  result in "smaller" repulsive sizes of atoms.
2. At each angle  $\theta$ , there is a minimal energy  $E_{Ar-X}(\theta)$  that an Ar must have in a head-on collision at angle  $\theta$  to sputter an S atom. This corresponds to the blue region on 5A

Combining the two, the blue region in Figure 13B represents pairs (head-on energy; angle) =  $(E_{Ar-X}, \theta)$  that would result in sputtering, while the purple region represents the accessible spread of reflection angles that are realized during an impact. Therefore, sputtering happens for those  $(E_{Ar-X}, \theta)$  values over which the two regions overlap, meaning that thermal fluctuations make the reflection angle spread wide enough to reach angles  $\theta$  that result in sputtering at a given energy.

Finally, the inherent  $\theta$ -spread of the projectiles is incorporated by using  $\sqrt{\theta_T(E_{Ar\perp})^2 + \theta_{inherent}^2}$  as the new  $\theta_T$ . Such simple quadratic addition of fluctuations is used because of 2 reasons. 1. The angles are small and therefore add approximately linearly. 2. The inherent and thermal  $\theta$  fluctuations are statistically independent, so their variances add linearly.

## Derivation details:

Derivation of eq.(3) - (5): Referring to Figure 16, we first transform to the center-of-mass(COM) frame as shown below:

$$m_O v_{CoM} = m_{Ar} (v_{Ar} - v_{CoM}) \Rightarrow v_{CoM} = \frac{m_{Ar} v_{Ar}}{m_{Ar} + m_O} \quad (6)$$

We then decompose the collision into a head-on collision along the line connecting the centers of Ar and O (thick dashed line in Figure 16) and the orthogonal direction, which

does not experience any changes after the collision. Along the head-on direction, we can write energy conservation to find the effective hard-sphere distance between Ar and O at their closest approach  $r_{Ar-O}$ :

$$\frac{m_O(v_{CoM} \cos(\theta))^2}{2} + \frac{m_{Ar}((v_{Ar} - v_{CoM}) \cos(\theta))^2}{2} = E_{collision} = U_{Ar-O}(r_{Ar-O}) \quad (7)$$

Relativistic corrections are neglected because  $v_{Ar}/c \sim 10^{-4}$  at  $E_{Ar\perp} \sim 10$  eV. Thus, the incoming Ar energy is  $E_{Ar\perp} = m_{Ar}v_{Ar}^2/2$ . Plugging everything in, we get

$$E_{collision} = \frac{E_{Ar\perp} \cos^2(\theta)}{1 + m_O/m_{Ar}} \quad (8)$$

which is what appears in eq.(3).

The derivation of eq.(2) follows directly from Figure 16: The triangle on points (Ar position; O current position; O equilibrium position) has the angle  $\theta$  and  $\pi/2$ , and sides  $\sigma_{xy,O}$  and  $r_{Ar-O}$ , thus  $\sin(\theta) = \sigma_{xy,O}/r_{Ar-O}$ , which is equivalent to eq.(2).

## Numerical solution for $E_{Ar\perp}(T)$ :

Equations (5) can be rewritten in a less intuitive form, which nevertheless simplifies mathematical analysis

$$\begin{cases} U_{Ar-X} \left( \frac{\sigma_{xy,X}(T)}{\sin(\theta_0)} \right) = \frac{E_{Ar-X}(\theta_0)}{1 + m_X/m_{Ar}} \Rightarrow \theta_0(\sigma_{xy,X}(T)) \\ E_{Ar\perp}(T) = E_{Ar\perp}(\theta_0(\sigma_{xy,X}(T))) = \frac{E_{Ar-X}(\theta_0)}{\cos^2(\theta_0)} \end{cases} \quad (9)$$

where  $X$  is the impacted atom type, which can be O/F/S.

A sufficient condition for solution uniqueness is  $\theta_0 < \theta_{opt}$  where  $\theta_{opt}(X) = \operatorname{argmin}_\theta(E_{Ar-X}(\theta))$ .

Oxygen is shown to satisfy at least  $\theta_{opt}(O) > 30^\circ$ . This gives the maximum applicable temperature condition

$$T < T_{max}(X) = \sigma_{xy,X}^{-1} \left[ \frac{\sin(\theta_{opt}(X)) U_{Ar-X}^{-1}(E_{Ar-X}(\theta_{opt}(X)))}{1 + m_X/m_{Ar}} \right] \quad (10)$$

We only need to consider  $U(r < r_{well})$ , where  $r_{well} = \text{argmin}_r[U(r)]$ , because this is the range that contains the hard-sphere distance  $r_{hard-sphere}$  that approximates the collision. The range  $r < r_{well}$  still covers the full range of energy values  $[0; \infty]$ , so both  $\sigma_{xy}(T)$  and  $U(r < r_{well})$  are always invertible. This is shown by shading the  $r > r_{well}$  on Figure 16B.

For oxygen, we can estimate  $T_{max}(\theta_{opt}(O)) > T_{max}(30^\circ) \approx 4900$  [K], which is beyond MoS<sub>2</sub> melting point of  $T_{melt} \sim 2650$  [K].<sup>63</sup> Therefore, the theory is formally valid for all physically relevant temperatures. In practice, the breakdown is expected to occur earlier, when the harmonic-well approximation  $\sigma_{xy}(T) \sim \sqrt{T}$ , used here to extrapolate  $\sigma_{xy}(T)$  in figure 14, begins to fail. A numerical evaluation of  $\sigma_{xy}(T)$ , would allow the applicable temperature range to be extended close to  $T_{melt}$ .

### High and low $T$ regimes of $E_{sputt}(T)$ :

The linear regime for low  $T$  comes from the fact that  $E_{Ar-X}(\theta)$  in Figure 4 is quadratic at the origin  $\theta = 0$ , and  $\cos(\theta)$  is also quadratic at  $\theta = 0$ . Thus, for temperatures  $T$  such that  $\theta_T \ll 1$  we can expand  $E_{Ar\perp}(T) \approx E_0(1 - \alpha\theta_T^2)$ . Next, we recall from eq.(4) that for low  $T$ ,  $\theta_T \approx \sigma_0/r_{Ar-X}(E_{Ar\perp})\sqrt{T/T_0}$ . The dependence of  $r_{Ar-X}(E_{Ar\perp})$  turns out to be weak for  $E_{Ar\perp} \sim 10$  eV, allowing us to approximate  $r_{Ar-X}(E_{Ar\perp}) \approx d_{atom,X} = const$  as shown below:

$$E_{Ar\perp}(T) \approx E_0 \left( 1 - \alpha \left( \frac{\sigma_0}{d_{atom,X}} \right)^2 \frac{T}{T_0} \right) = E_0 - bT \quad (11)$$

The plateau regime is more incidental. It occurs when the decrease in  $E_{Ar-X}(\theta_T)$  is compensated by the decrease in  $\cos^2(\theta_T)$ . It is wide compared to the linear region because  $\sigma_{xy}(T) \propto \sqrt{T}$  changes more slowly at higher  $T$ , and  $E_{Ar-X}(\theta)$  likewise varies more slowly at higher  $\theta$ . The transition from the linear regime happens at  $T_{switch}$  when  $E''_{Ar-X}(\theta)$  deviates from its initial parabolic shape, meaning the curvature  $E''_{Ar-X}(\theta_{T_{switch}})$  becomes significantly

different from  $E''_{Ar-X}(0)$ .

The theoretical prediction in Figure 5 is not followed exactly within the error-bars, which can be due to several approximations. For very small  $\theta$ , the two-body approximation may break down, since the impacted O/F atom is pushed almost directly into the S atom below it, making the process at least a three-body problem. Too wide angles  $\theta \sim 1$  may start to break the hard-sphere collision model because higher  $\theta$  leads to longer periods before the main collision when the Ar already feels the material below, which may alter its course in a more complicated way.

## Spin treatment:

Treating spins breaks down into two separate questions that are distinguished by their timescales: the appropriate equilibrium initial states and the appropriate dynamics during and after the collision. First, we explain why singlet initial states were chosen, and then why we decided fixed spin singlet dynamics to be the optimal choice between computational cost and accuracy for dynamics.

First, we note that we used CP2K<sup>64-73</sup> to obtain results presented in this work, and we are only aware of global spin fixation within this framework. This can lead to unpaired electrons localizing on parts of the system where they are not desired, such as the impacting argon atom. Impacts with metastable projectiles can happen in reality, but are beyond the scope of this work. Simulating Ar impacts in a fixed triplet state lowers the sputtering thresholds relative to singlet results. However, the ground states of 2H phases of MoS<sub>2</sub>, MoS<sub>2</sub>O and MoS<sub>2</sub>F are singlets (meaning these materials are not ferromagnetic). Thus, initializing the system in a triplet state puts it in an excited state configuration. We estimate it to be  $\sim 1.8$  eV above the ground state for a 4x4 single-layer MoS<sub>2</sub> + Ar system.

Oxygen is known to exhibit non-trivial spin effects, for example, its molecular form O<sub>2</sub> is known to have a triplet ground state. Figure 8B red lines show PES for an O atom at varying

distances from  $\text{MoS}_2$ . It is significantly different for singlet (solid) and triplet (dashed) spin states of the systems. All simulations reported in the main text were performed in a fixed-spin singlet state, which may pose a question about their validity, since potential oxygen dissociation from  $\text{MoS}_2\text{O}$  can play a significant role in the processes investigated in this work. However, we provide the following qualitative arguments for why simulating impacts in a fixed singlet state represents an optimal choice between computational cost and accuracy:

1. The main ejection product for  $\text{MoS}_2\text{O}$  is  $\text{SO}_2$ , which has a singlet ground state. We simulated fixed-triplet Ar bombardment of  $\text{MoS}_2\text{O}$  and the dominant product was still  $\text{SO}_2$ . The sputtering threshold in fixed-triplet simulations decreased by  $(2 \pm 0.5)$  eV. This is consistent with our observation that the total system energy in the triplet state is 1.8 eV higher than in the singlet state, corresponding to an "unpairing excitation" of 1.8 eV.
2. Oxygen singlet is a ground state when attached to  $\text{MoS}_2$  (Figure 8B) and it follows the singlet PES at least until  $r_{S-O} \approx 2.15$  Å. Triplet becomes lower at larger  $r$ , which might be relevant for atomic O sputtering, for example during oxygen cleaning from the TMD after processing. However, we do not focus on O sputtering in this work.
3. While the triplet becomes lower than singlet for  $r > 2.15$  Å, we believe that fix-spin dynamics is appropriate even for the impacts simulated here, because of the spin-relaxation dynamics of oxygen:
  - (a) While estimating de-excitation time of a specific atomic O near a TMD has not been studied previously, we can try to get insight from molecular oxygen. Given a singlet state,  $\text{O}_2$  requires  $\approx 20\mu\text{s}$  to de-excite to a triplet state.<sup>74,75</sup> This is about  $\sim 7$  orders of magnitude longer than the "immediate" sputtering processes (excluding long-term thermal desorption of products) considered in this work.
  - (b) The  $20\mu\text{s}$  estimate is under near-ambient conditions relative to  $\sim 10$  eV collisions, which is a significant difference because de-excitations can only happen via

relatively strong interactions coupling spin degrees of freedom to the rest of the system. Strong collisions can provide such coupling. Estimating de-excitation probabilities from collisions can be done in principle,<sup>76</sup> however, we did not perform such in-depth analysis because:

- (c) Robust de-excitation to a triplet state can only occur at nuclei positions where the triplet electronic state is the ground state. This is not the case for O atoms attached to MoS<sub>2</sub> and remains true until  $r_{S-O} = 2.15 \text{ \AA}$  (Figure 8B). Therefore, the main Ar-O collision happens while O is in a position where its ground state is a singlet, thus it is not converted into a triplet.
- (d) By the time the impacted O has moved more than 2.15  $\text{\AA}$  away from the top S-layer, the impact energy has likely dissipated into many surrounding atoms, and no single collision is likely to be sufficiently energetic to provide strong spin-electronic coupling capable of inducing a spin-flip.

## DFT applicability:

The Born–Oppenheimer (BO) approximation assumes that electrons remain in their ground state for each nuclear configuration, which requires that nuclei move much more slowly than electrons. An order of magnitude estimate for the lower boundary of electron velocity in atoms is the atomic unit  $v_e = \alpha c$ , where  $c$  is the speed of light and  $\alpha = e^2/\hbar c \approx 1/137$ . An Ar atom moving at  $v = v_e$  has a kinetic energy of  $\approx 1 \text{ MeV}$ , which is far greater than 10 eV. All other energies in the collision are smaller than this, so the BO approximation should hold well during the whole process.

The ground-state approximation is more complicated. A necessary condition for it is the prevalence of ionic stopping power relative to electronic one. It was experimentally shown for ice bombardment with He+ ions that ion energies below  $\sim 1 - 2 \text{ keV}$  are dominated by ionic scattering.<sup>77</sup> One reason for this is the highly non-unitary mass ratio between electrons and

ions, which suppresses fast energy transfer between ionic and electronic degrees of freedom.

However, excitations can be transferred directly into the electronic degrees of freedom of the material by several channels, such as impacts of excited atoms ( $\text{Ar}^*$ ) and/or neutralization of the projectile shortly before impact. The latter can also be viewed as a special case of de-excitation, since a charged particle (ion) near a material with much higher capacitance is in an excited state. De-excitations can occur through a number of Auger and resonant like channels.<sup>33</sup> The resonant channel may not result in excitations because the electron transitions between states at the same energy level. It has been shown to dominate for  $\text{Ne}^+$  neutralization during  $\text{MoS}_2$  bombardment at  $E \leq 2$  keV due to a match between the electronic band structure of  $\text{MoS}_2$  and the electronic levels of  $\text{Ne}^+$ .<sup>32</sup> This is not always the case, for example  $\sim 1/5$   $\text{He}^+$  ions caused electron ejections from ice at  $E_{ion} = 10$  eV<sup>78</sup> due to Auger neutralization. In this work, we do not account for excitations, which may affect quantitative results such as the absolute value of  $E_{sputt}$ . However, the qualitative relative results, such as different sputtering mechanisms and the decrease in  $E_{sputt}$  they induce do rely on simple physical explanations rather than DFT results alone, and we therefore expect them to hold in reality.

## DFT details:

We used UZH pseudo-potentials GTH-GGA<sup>79</sup> and the corresponding basis sets TZV2P-MOLOPT-GGA-GTH,<sup>68</sup> as they are an update to the default CP2K GTH choice optimized for heavier elements such as transition metals and for mGGA functionals like R2SCAN, which we employed in several parts of this work. The Gaussian plane wave (GPW) method was used for propagation.<sup>79-83</sup> The CUTOFF and REL-CUTOFF parameters were converged to 400 Ry and 40 Ry, respectively, corresponding to an energy error tolerance of  $\sim 10^{-2}$  H following the official CP2K guidelines. Achieving a tolerance of  $\sim 10^{-3}$  H would require 700 Ry and 60 Ry respectively. Given the energy scale of our processes  $\sim 10$  eV with  $\Delta E/E \sim 0.1$ , we

selected the coarser  $\sim 10^{-2}$  H accuracy. ASPC extrapolation was used to predict the next step density.<sup>84,85</sup> Quickstep EPS was set to  $10^{-8}$ , SCF EPS to  $10^{-5}$  and orbital transformation (OT) diagonalization<sup>86</sup> was used with a FULL-SINGLE-INVERSE preconditioner and DIIS optimizer.<sup>87</sup> All considered TMDs are not metallic and/or magnetic, which allowed us to avoid smearing. A potential interaction cutoff of 10 Å was applied, and a time integration step of 1 fs was used. Impact simulations were performed in NVE ensemble to accurately capture energy transfer between system components and dynamics. Each simulation was run for 2 ps after the impact, as justified in the main text. Equilibration was performed in the  $NP_{xy}L_zT$  ensemble and propagated until convergence. The initial Z-distance of Ar atom from the top TMD layer was set to 10 Å.

Figure 8A shows only a negligible difference between the PBE<sup>88</sup> and R2SCAN<sup>89</sup> functionals for the PES, both in terms of adsorption energies and overall profiles. Dispersion corrections using rVV10<sup>90</sup> versus D3BJ<sup>91</sup> also show negligible differences. Therefore, we use the simplest option, PBE-D3. This choice is also commonly adopted in the literature for MoS<sub>2</sub> + O systems.<sup>14,46,55</sup> The R2SCAN functional combined with rVV10 dispersion was included for comparison because more sensitive properties, such as phonon spectra of MoS<sub>2</sub> has been shown to require R2SCAN + rVV10 for accurate description.<sup>92</sup> Our claim of a low adsorption energy barrier for atomic O and F is somewhat affected by the functional: PBE predicts a barrier closer to 0.1 eV, while R2SCAN yields a value closer to 0.2 eV. However, both values are comparable to ambient thermal energy  $k_B T \sim 0.026$  eV. Therefore, the claim of unimpeded adsorption is likely justified.

## Free-energy simulation setup:

We used CP2K + PLUMED (the open-source, community-developed PLUMED library,<sup>93</sup> version 2.x<sup>94</sup> or alternatively version 1.x.<sup>95</sup>) to run meta-dynamics (metaD).<sup>96,97</sup> A 2x2 supercell with a single adsorbed O or F atom was employed. The distance between the

adsorbing O/F atom  $Z_{O/F}$  and the center of mass of the entire TMD layer  $Z_{TMD}$ , was chosen as the collective variable ( $CV = \delta Z = Z_{TMD} - Z_{O/F}$ ) for metaD. We bias the Z-coordinate of the TMD layer to a fixed value with a parabolic potential  $k_{TMD}(Z_{TMD} - Z_0)^2/2$  with  $k_{TMD} = 2.5 \text{ eV}/\text{\AA}^2$ . From unconstrained equilibration runs, we find that the stable bonding sites for both O and F are approximately on top of the corresponding S atoms. Therefore, we applied another parabolic bias ( $k = 5 \text{ eV}/\text{\AA}^2$ ) on  $X_{O/F} - X_{S,bond}$  and  $Y_{O/F} - Y_{S,bond}$  to prevent the O/F from slipping off the bonding S atom under the pressure of the metaD bias. Finally, we applied one sided parabolic walls on  $\delta Z$  at  $1.5 \text{ \AA}$  ( $k = 3 \text{ eV}/\text{\AA}^2$ ) and  $8 \text{ \AA}$  ( $k = 1 \text{ eV}/\text{\AA}^2$ ) to prevent pushing the formed S-O/F bond into the layer and to avoid exploration of non-interacting regions and artifacts due to periodic boundary conditions. Gaussian of width  $0.1 \text{ \AA}$  and height of  $0.03 \text{ eV}$  ( $\sim k_B T$  to avoid trapping the CV) are deposited every  $100 \text{ fs}$  ( $\sim$  couple thermal motions of O/F in its potential well). A Bias-factor of  $\gamma = 100$  was chosen  $\approx E_{desorb}/k_B T$  assuming a desorption barrier  $E_{desorb} \sim 2 - 4 \text{ eV}$  and  $T = 300 \text{ K}$ . Convergence analysis was performed according to the official guidelines (see Figures 8C and 8F). Convergence times, shown in the titles of Figures 8D and 8E, are  $\sim 20 - 30 \text{ ps}$ . Each metaD calculation was run for at least  $100 \text{ ps}$ .

## Figures:

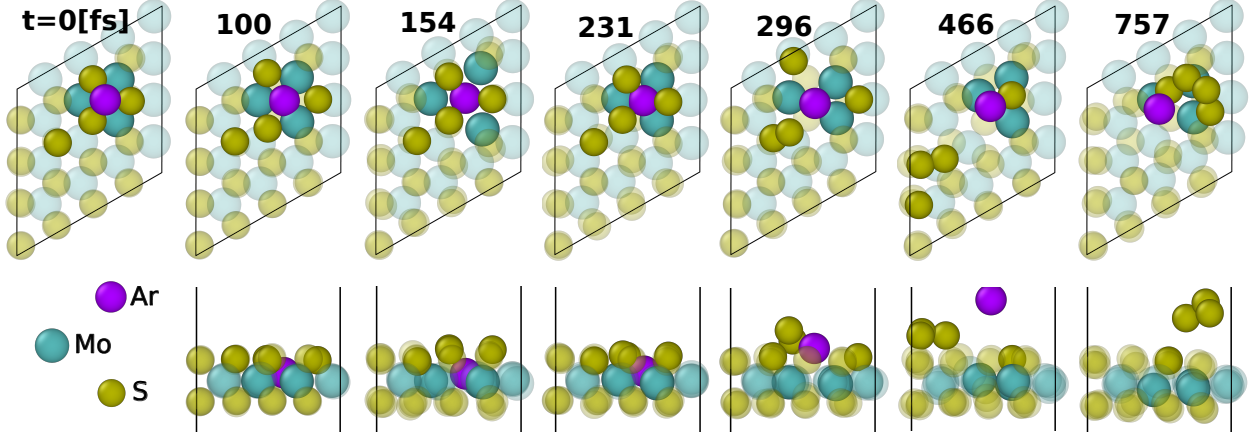


Figure 6: Typical sputtering of pristine  $\text{MoS}_2$  at  $E_{\text{Ar}\perp} = 34$  eV. Video is given in video V2. (Top) plane view, (Bottom) side view. Gray numbers indicates timestamps in [fs]. The Ar atom has enough energy to penetrate through the top S layer and push apart Mo atoms (154 fs). These Mo atoms later push the Ar atom back out of the lattice as following: First (231 fs), Ar remains located “within” the Mo layer, but the Mo atoms return from their displaced state with an increased spacing because of the incorporated argon atom.(at 154 fs). Then, the rebounding Molybdenum atoms strongly drive the Ar atom forward, which then collides with the top-layer S atoms at 296 fs. The displaced S-s subsequently combine to form an  $\text{S}_3$  species that then depart. Using a search similar to one described in Figure 9, we showed that this mechanism is the most energy efficient.

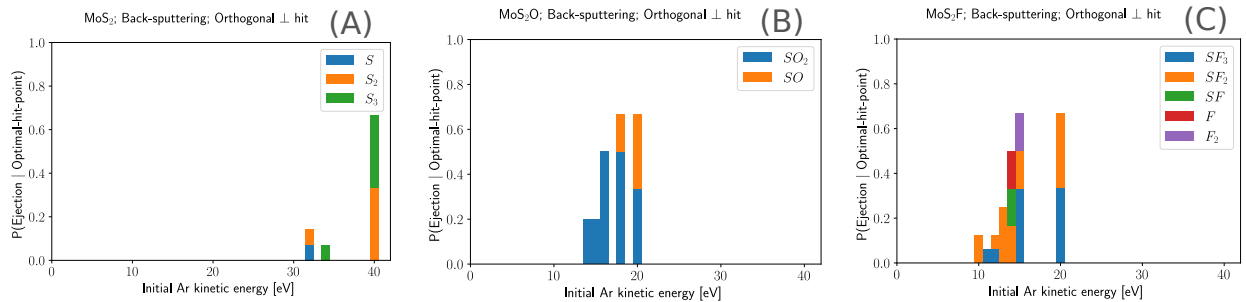


Figure 7: Breakdown of sputtering probabilities from Figure 2 by products. This further illustrates a more clean sputtering nature for  $\text{MoS}_2\text{O}$  compared to more noisy sputtering observed for  $\text{MoS}_2\text{F}$ .

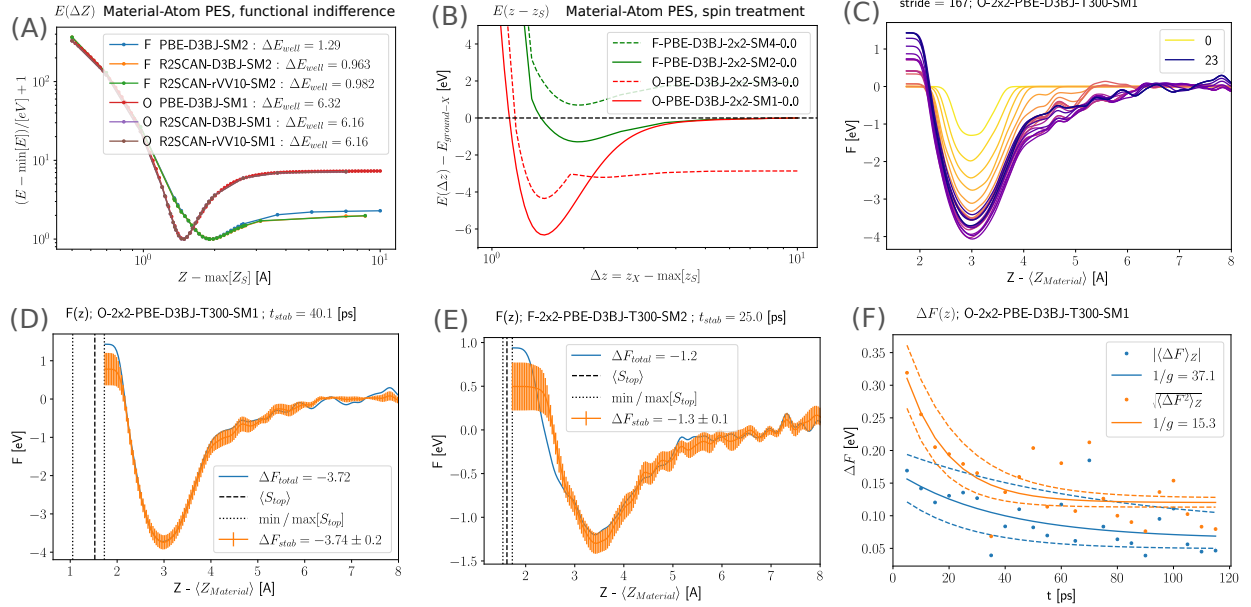


Figure 8: Calculations for O and F adsorption on MoS<sub>2</sub>. (A) Potential energy profiles for placing an Oxygen (red-like) or Fluorine (green-like) atom at different distances from the top sulfur layer of a geometry-optimized MoS<sub>2</sub> 2x2 single layer. The close agreement between R2SCAN and PBE curves indicates that using a mGGA is not essential. Similarly, the R2SCAN-rVV10 and R2SCAN-D3BJ curves suggest no significant advantage of rVV10 over D3BJ dispersion correction. (B) Spin-states analysis in a setup similar to A. Oxygen is red, Fluorine is green. Abrupt changes at small  $r$  are because we focused on plotting near-the-well points. Solid lines are what is used in AIMD collision simulations. Spin-excited (quintuplet) F-case is higher than duplet everywhere. The O-case triplet becomes the ground state at  $r > 2.15 \text{ \AA}$ . However, O is clearly a singlet when adsorbed, and there are no metastable states near  $r = 2.15 \text{ \AA}$ , which suggests O will be near  $r = 2.15 \text{ \AA}$  only for short times, making the spin-flips unlikely. The triplet PES is useful to confirm the previously reported dissociation barrier of  $\sim 1.3 \text{ eV}$ . (C) Free-energy profile of an oxygen atom as a function of its distances from the center-of-mass of a 2x2 MoS<sub>2</sub> single layer. Dynamics are run with unconstrained spin to test whether dynamical spin polarization affects the profile near the singlet-triplet degeneracy region. (D) Same as (c), but for a fluorine atom. (E) A typical time-evolution of meta-dynamics free-energy profile. (F) A typical convergence analysis for meta-dynamics.

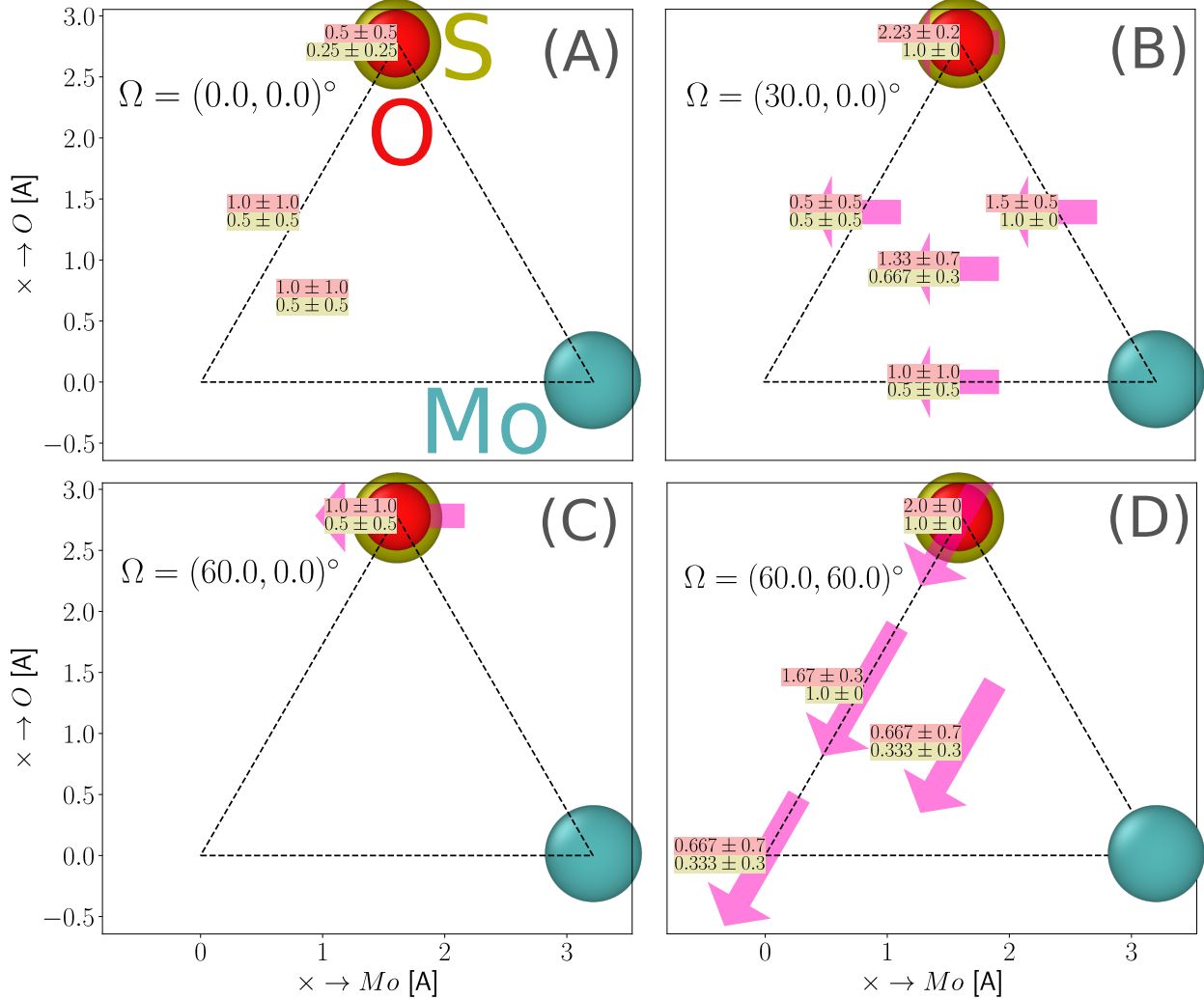


Figure 9: Finding the most damage-susceptible point of  $\text{MoS}_2\text{O}$ . Impacts are performed at  $E_{\text{Ar}} = 15$  eV. The triangle on each scheme corresponds to the purple triangle in Figure 1D, oriented according to the S and Mo atom labels. Thick purple arrows indicate projections of the initial Ar velocity. Different hit-points and impact angles are surveyed (A-D). The only hit-point that always results in sulfur sputtering is directly above sulfur, corresponding to a head-on impact on oxygen in its equilibrium position.

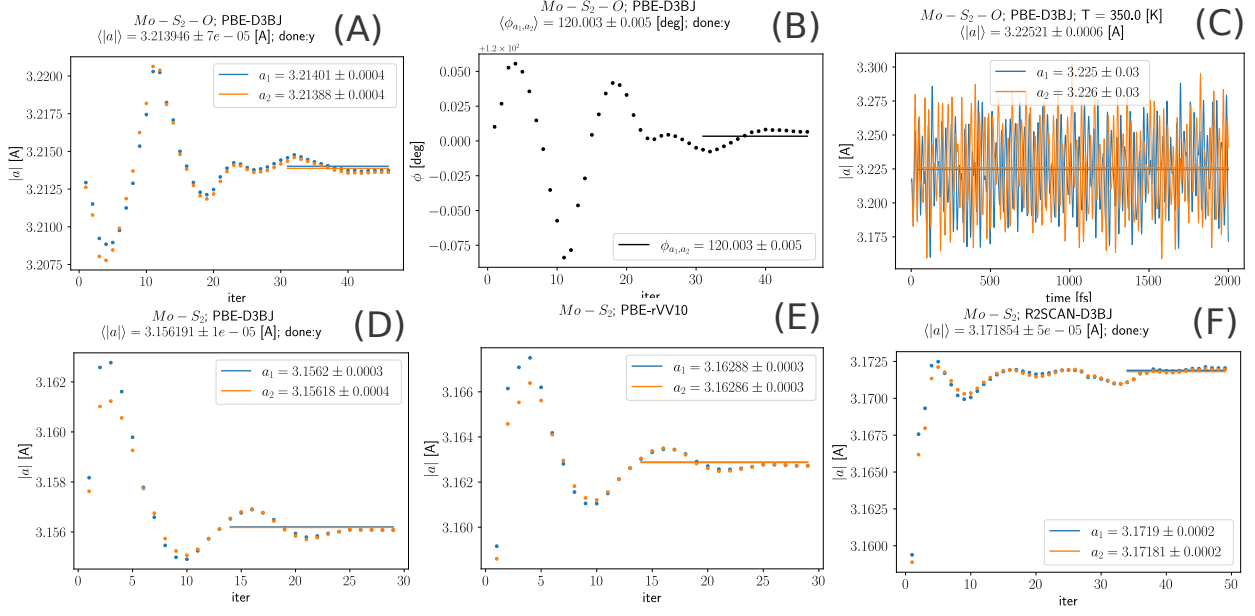


Figure 10: Equilibration before impact illustrated for MoS<sub>2</sub>O. Geometry optimization was performed in the  $NP_{xy}L_zT$  ensemble to allow the unit cell to break three-fold symmetry while preventing the collapse along the  $Z$  direction. (A) Evolution of both lattice constants during optimization. (B) Evolution of the angle between the lattice constant vectors. (C)  $NP_{xy}L_zT$  AIMD trajectory confirming that the ground-state optimization result from (A) is close to the lowest free-energy state. (D) Geometry optimization of MoS<sub>2</sub>. (E) Same as (D), but including rVV10 dispersion with parameters for TMDs.<sup>92,98</sup> The results in fact deviate even more from the experimental value of  $\sim 3.15$  Å.<sup>99</sup> (F) Same as (D), but using R2SCAN functional with D3 dispersion parameters optimized for TMDs.<sup>92</sup>

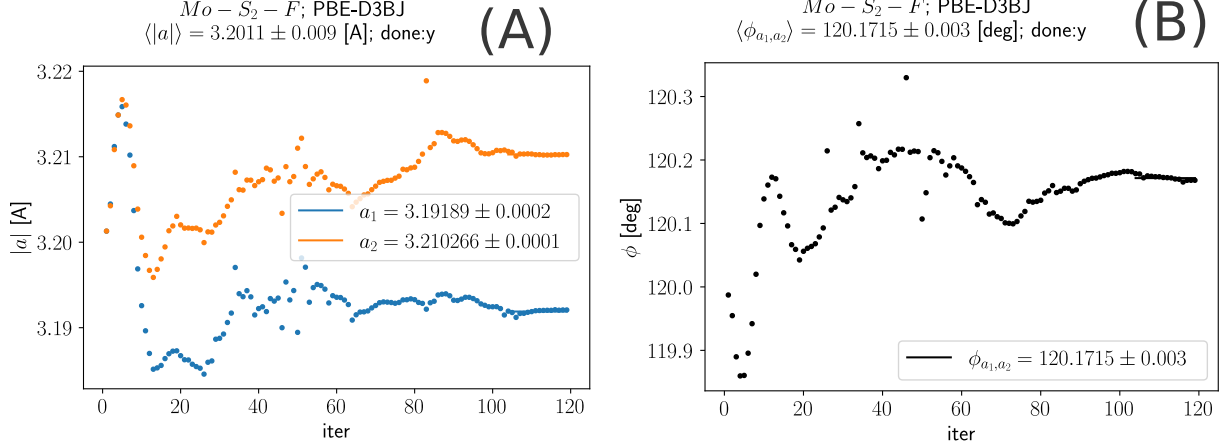


Figure 11: Geometry optimization of MoS<sub>2</sub>F. PBE+D3 is chosen based on its comparison to alternatives in Figure 10. (A) Lattice constants evolution. Spontaneous symmetry breaking is observed, as the lattice constants differ well beyond the error bars. (B) Angle between lattice constant vectors, which also deviates significantly from 120° beyond the error bars.

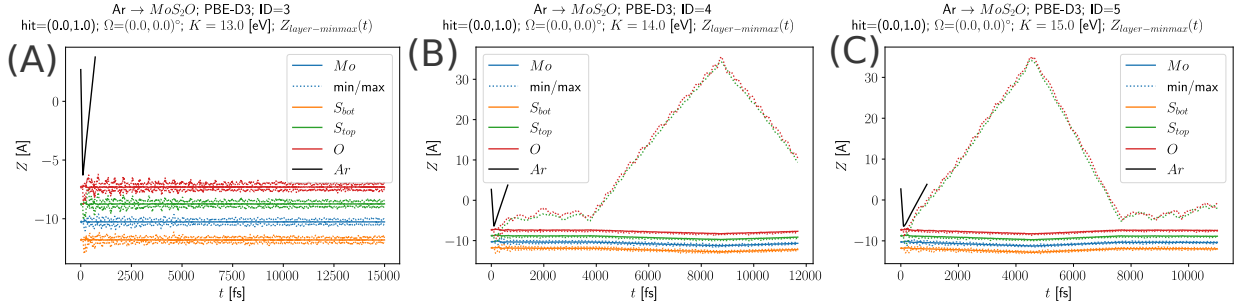


Figure 12: Sample longer AIMD runs verifying that a 2ps simulation time used for most production results is sufficient to identify immediate sputtering events. Red, Green, Blue, and Yellow correspond to the O,  $S_{top}$ , Mo, and  $S_{bot}$  layers. Dotted lines indicate the maximum and minimum Z-coordinates within each layer. An  $\text{SO}_2$  forms on (B) at 14 eV, but takes several ps to desorb, while an impact energy of 15 eV is sufficient for immediate sputtering. In general, removal of sputtered products involves an activation process that can occur on a much longer timescale. However, such products can also form through mechanisms other than Ar impacts and would require a different analysis, which is beyond the scope of this work.

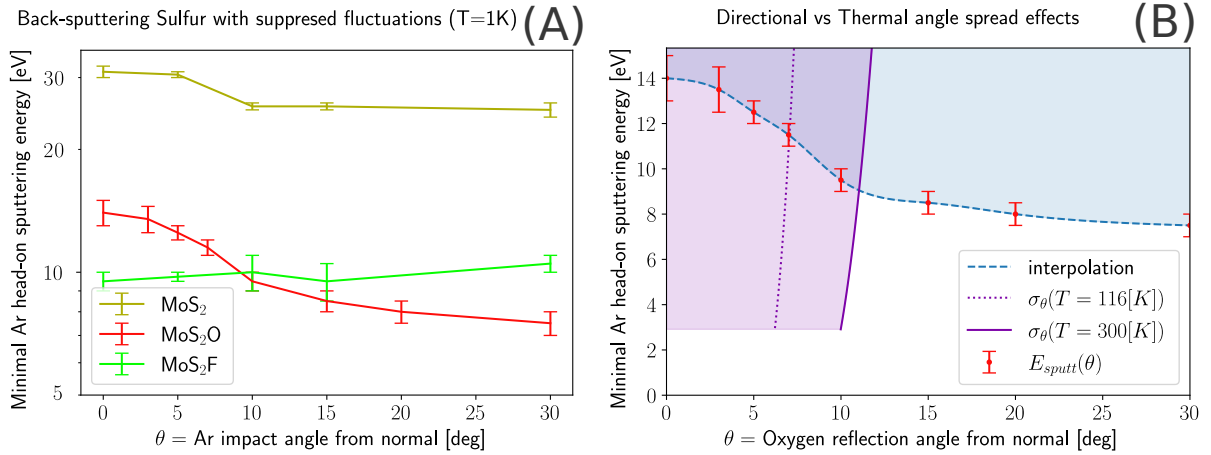


Figure 13: (A) Angular dependence of the sputtering threshold energy  $E_{sputt}$  for pristine (dark yellow), fluorinated (light green) and oxygenated (red)  $\text{MoS}_2$  under normal hits. Such fluctuations are suppressed by setting  $T = 1\text{K}$ . Each curve is obtained after optimizing the in-plane angle  $\varphi$  to minimize  $E_{sputt}$ , as shown for  $\text{MoS}_2\text{O}$  in Figure 15. Simulations at  $\theta = 45^\circ$  for  $\text{MoS}_2$  and  $\text{MoS}_2\text{O}$  yielded  $E_{\text{MoS}_2}(45^\circ) > 35$  eV and  $E_{\text{MoS}_2\text{O}}(45^\circ) > 14$  eV. (B) Sputtering possibility diagram for  $\text{MoS}_2\text{O}$ . Red datapoints indicate the Ar energy threshold for sulfur ejections in non-normal head-on Ar-O collisions with suppressed thermal fluctuations ( $T=1\text{[K]}$ ). The Blue dashed line shows a smooth (cubic) interpolation of the red data, and the blue shaded region marks where sputtering occurs. The solid purple line and corresponding shade represent the range of reflection angles  $\theta$  that an O atom is likely to acquire after a Ar normal impact at  $T = 300\text{[K]}$ , while the Purple-dotted line shows the thermal spread  $\theta_T$  accessible at  $T = 116$  [K]. Overlap between the blue and purple regions indicates where sputtering from normal impacts is expected.

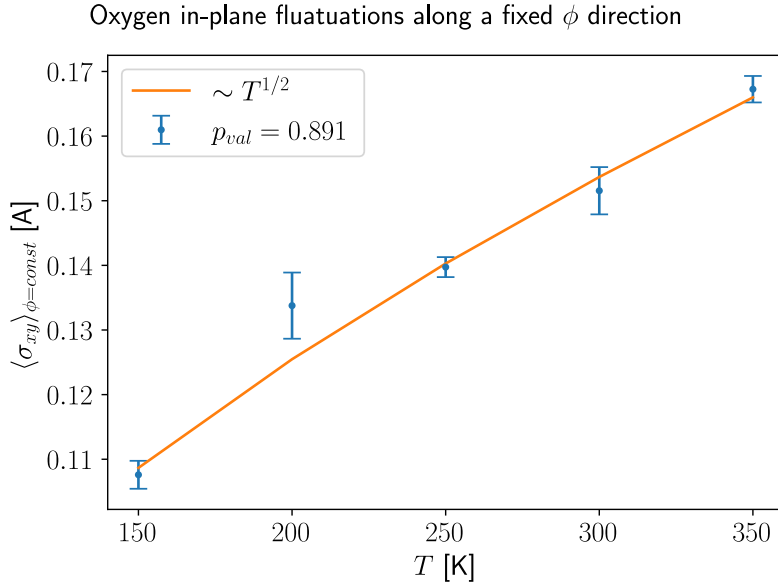


Figure 14: Magnitude of in-plane thermal fluctuations of oxygen atoms adsorbed on MoS<sub>2</sub>. The  $\sim T^{1/2}$  scaling follows from approximating the adsorbed atoms as confined in an approximately harmonic square well potential, which implies  $\sigma_{xy}^2 \sim \langle U \rangle = \langle K \rangle \sim k_B T$  by the virial theorem. The high p-value indicates that the  $T^{1/2}$  scaling provides a good description of the data. We redefine  $\sigma_{xy,\phi=const}^2 = (\sigma_x^2 + \sigma_y^2)/2$ , where the factor 1/2 reflects that we are only interested in fluctuations along a relatively narrow range of in-plane angles  $\phi \approx \phi_{opt}$ . Only this range is susceptible to damage near the sputtering threshold  $E_{sputt}$ , as shown in Figure ref fig:F4S2. We also assumed that in-plane fluctuations have the same magnitude in any in-plane direction, which is probably not exactly accurate because of in-plane inhomogeneity. However,  $\sigma_x$  was found to be within error-bars of  $\sigma_y$  in repeated simulations, which justifies computing a simple average for  $\sigma_{xy,\phi=const}^2$ .

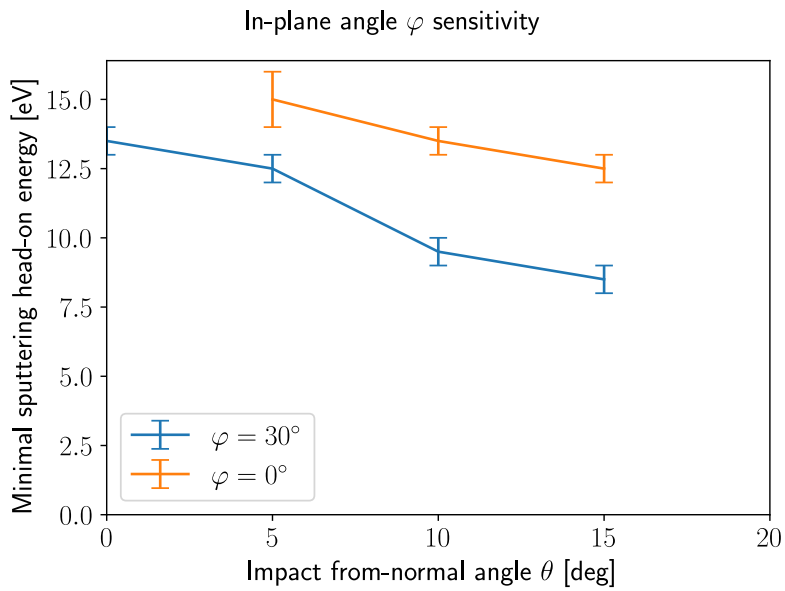


Figure 15: Importance of the in-plane impact angle  $\varphi$  for  $\text{MoS}_2\text{O}$ . Clearly higher energies are required for sputtering at  $\varphi = 0^\circ$  than at  $30^\circ$ . We note that the curves do not have to be monotonic, at least for all  $\varphi \neq \varphi_{opt}$ , since pushing an O more into the wrong direction  $\varphi$  can further complicate the sputtering process. We also note that the curves do not have to meet at  $\theta = 0$  if fluctuations are suppressed because even an infinitesimal tilt in the wrong direction may complicate sputtering. In the presence of thermal fluctuations, the curves should meet for angles smaller than the thermal angular spread  $\theta < \theta_T(E_{Ar\perp})$ .

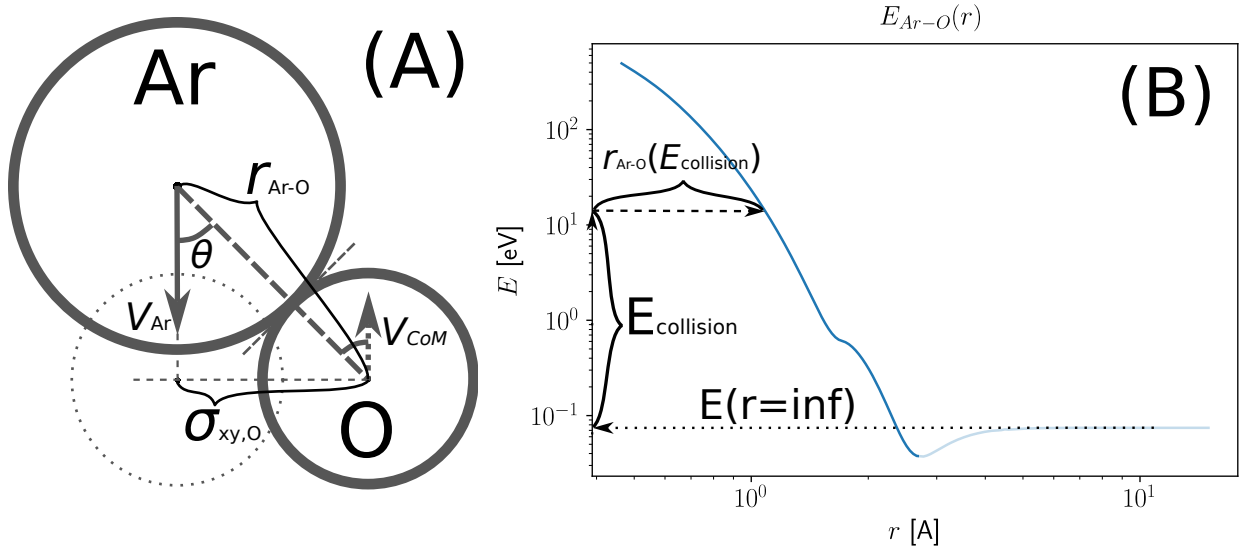


Figure 16: Ar-O collision schematic. (A) Hard-sphere Ar-O collision model. The dotted circle is the equilibrium O position, while the O circle shifted by  $\sigma_{xy,O}$  to the right represents its position at the moment of impact with Ar. The collision plane (thin dashed line) is orthogonal to the line through the centers of Ar and O (thick dashed). The incoming Ar has velocity  $V_{Ar}$ , however treating the collision in the CoM frame assigns the O atoms a velocity  $V_{CoM}$  and subtracts the same  $V_{CoM}$  from  $V_{Ar}$ . Because  $\sigma_{xy,O} \sim r_{Ar-O}$  we get non-negligible  $\theta = \arcsin(\sigma_{xy,O}/r_{Ar-O})$ . A non-head-on collision can always be decomposed into a head-on collision and a fly-by (orthogonal to the head-on collision). (B) Two-atom potential energy profile  $U_{Ar-O}(r)$  for Ar-O used in eq.(3). The value of  $r_{Ar-O}$  is found as  $U_{Ar-O}^{-1}(E_{collision})$ . See the Supplementary information for the derivation of  $E_{collision}$ .

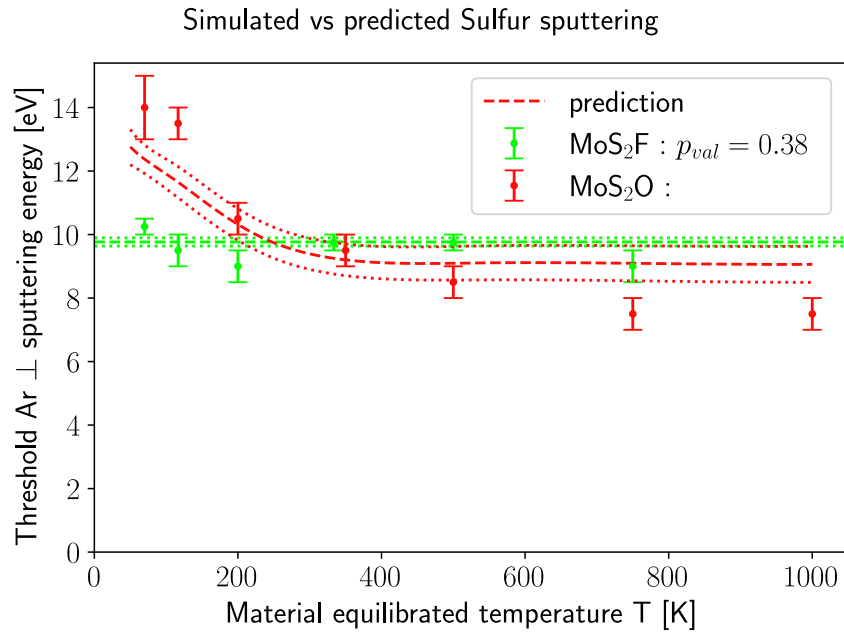


Figure 17: Confirmation of the theoretical prediction in Figure 5 at  $\theta_{inherent}$  with AIMD simulation results. Red and green correspond to MoS<sub>2</sub>O and MoS<sub>2</sub>F respectively. Data points indicate sputtering thresholds obtained from direct MD simulations at given temperatures. Dashed lines show the solution  $E_{Ar\perp}(T)$  of eq.(5). Dotted lines represent confidence intervals estimated from  $E_{Ar-X}$  error-bars. Error bars reflect the step of the energy grid used to pin down the threshold. No fitting parameters were used (with the exception of the spline parameters used for interpolating spline data of  $E_{Ar-X}(\theta)$  from Figure 4).

## References

- (1) Michael Nastasi, J. K. H., James W. Mayer *Ion Solid Interactions: fundamentals and applications*; Cambridge University Press, 1996.
- (2) Nanda, G.; Hlawacek, G.; Goswami, S.; Watanabe, K.; Taniguchi, T.; Alkemade, P. F. Electronic transport in helium-ion-beam etched encapsulated graphene nanoribbons. *Carbon* **2017**, *119*, 419–425.
- (3) Lemme, M. C.; Bell, D. C.; Williams, J. R.; Stern, L. A.; Baugher, B. W. H.; Jarillo-Herrero, P.; Marcus, C. M. Etching of Graphene Devices with a Helium Ion Beam. *ACS Nano* **2009**, *3*, 2674–2676.
- (4) Archanjo, B. S.; Barboza, A. P. M.; Neves, B. R. A.; Malard, L. M.; Ferreira, E. H. M.; Brant, J. C.; Alves, E. S.; Plentz, F.; Carozo, V.; Fragneaud, B.; Maciel, I. O.; Almeida, C. M.; Jorio, A.; Achete, C. A. The use of a Ga+focused ion beam to modify graphene for device applications. *Nanotechnology* **2012**, *23*, 255305.
- (5) Wang, D.; Wang, Y.; Chen, X.; Zhu, Y.; Zhan, K.; Cheng, H.; Wang, X. Layer-by-layer thinning of two-dimensional MoS<sub>2</sub>films by using a focused ion beam. *Nanoscale* **2016**, *8*, 4107–4112.
- (6) Stanford, M. G.; Pudasaini, P. R.; Cross, N.; Mahady, K.; Hoffman, A. N.; Mandrus, D. G.; Duscher, G.; Chisholm, M. F.; Rack, P. D. Tungsten Diselenide Patterning and Nanoribbon Formation by Gas-Assisted Focused-Helium-Ion-Beam-Induced Etching. *Small Methods* **2017**, *1*.
- (7) Bertolazzi, S.; Bonacchi, S.; Nan, G.; Pershin, A.; Beljonne, D.; Samorì, P. Engineering Chemically Active Defects in Monolayer MoS<sub>2</sub> Transistors via Ion-Beam Irradiation and Their Healing via Vapor Deposition of Alkanethiols. *Advanced Materials* **2017**, *29*.

(8) Chow, P. K.; Jacobs-Gedrim, R. B.; Gao, J.; Lu, T.-M.; Yu, B.; Terrones, H.; Koratkar, N. Defect-Induced Photoluminescence in Monolayer Semiconducting Transition Metal Dichalcogenides. *ACS Nano* **2015**, *9*, 1520–1527.

(9) Lin, Z.; Carvalho, B. R.; Kahn, E.; Lv, R.; Rao, R.; Terrones, H.; Pimenta, M. A.; Terrones, M. Defect engineering of two-dimensional transition metal dichalcogenides. *2D Materials* **2016**, *3*, 022002.

(10) Fox, D. S. et al. Nanopatterning and Electrical Tuning of MoS<sub>2</sub> Layers with a Sub-nanometer Helium Ion Beam. *Nano Letters* **2015**, *15*, 5307–5313.

(11) Ma, L.; Tan, Y.; Ghorbani-Asl, M.; Boettger, R.; Kretschmer, S.; Zhou, S.; Huang, Z.; Krasheninnikov, A. V.; Chen, F. Tailoring the optical properties of atomically-thin WS<sub>2</sub> via ion irradiation. *Nanoscale* **2017**, *9*, 11027–11034.

(12) Sovizi, S.; Angizi, S.; Ahmad Alem, S. A.; Goodarzi, R.; Taji Boyuk, M. R. R.; Ghanbari, H.; Szoszkiewicz, R.; Simchi, A.; Kruse, P. Plasma Processing and Treatment of 2D Transition Metal Dichalcogenides: Tuning Properties and Defect Engineering. *Chemical Reviews* **2023**, *123*, 13869–13951.

(13) Lu, W.; Birmingham, B.; Zhang, Z. Defect engineering on MoS<sub>2</sub> surface with argon ion bombardments and thermal annealing. *Applied Surface Science* **2020**, *532*, 147461.

(14) Ma, Q. et al. Controlled argon beam-induced desulfurization of monolayer molybdenum disulfide. *Journal of Physics: Condensed Matter* **2013**, *25*, 252201.

(15) Gutiérrez, H. R.; Perea-López, N.; Elías, A. L.; Berkdemir, A.; Wang, B.; Lv, R.; López-Urías, F.; Crespi, V. H.; Terrones, H.; Terrones, M. Extraordinary Room-Temperature Photoluminescence in Triangular WS<sub>2</sub> Monolayers. *Nano Letters* **2012**, *13*, 3447–3454.

(16) Wang, Y.; Dai, H.; Liu, Z.; Liu, D. Phonon Scattering in Monolayer Molybdenum Disulfide. *Journal of Physics: Condensed Matter* **2013**, *25*, 252202.

fide under Different Defect Concentrations Based on Temperature-Dependent Raman Spectra. *The Journal of Physical Chemistry C* **2023**, *127*, 1109–1116.

(17) Bae, S.; Sugiyama, N.; Matsuo, T.; Raebiger, H.; Shudo, K.-i.; Ohno, K. Defect-Induced Vibration Modes of Ar+ - Irradiated MoS<sub>2</sub>. *Physical Review Applied* **2017**, *7*.

(18) Parkin, W. M.; Balan, A.; Liang, L.; Das, P. M.; Lamparski, M.; Naylor, C. H.; Rodríguez-Manzo, J. A.; Johnson, A. T. C.; Meunier, V.; Drndić, M. Raman Shifts in Electron-Irradiated Monolayer MoS<sub>2</sub>. *ACS Nano* **2016**, *10*, 4134–4142.

(19) Park, J.; Jung, J.; Kim, M.-S.; Lim, C.-M.; Choi, J.-E.; Kim, N.; Kim, J.-H.; Chung, C.-W. Damage-Free Plasma Source for Atomic-Scale Processing. *Nano Letters* **2024**, *24*, 11462–11468.

(20) Komsa, H.-P.; Kotakoski, J.; Kurasch, S.; Lehtinen, O.; Kaiser, U.; Krasheninnikov, A. V. Two-Dimensional Transition Metal Dichalcogenides under Electron Irradiation: Defect Production and Doping. *Physical Review Letters* **2012**, *109*.

(21) Kretschmer, S.; Lehnert, T.; Kaiser, U.; Krasheninnikov, A. V. Formation of Defects in Two-Dimensional MoS<sub>2</sub> in the Transmission Electron Microscope at Electron Energies below the Knock-on Threshold: The Role of Electronic Excitations. *Nano Letters* **2020**, *20*, 2865–2870.

(22) Yoshimura, A.; Lamparski, M.; Giedt, J.; Lingerfelt, D.; Jakowski, J.; Ganesh, P.; Yu, T.; Sumpter, B. G.; Meunier, V. Quantum theory of electronic excitation and sputtering by transmission electron microscopy. *Nanoscale* **2023**, *15*, 1053–1067.

(23) Novko, D.; Blanco-Rey, M.; Alducin, M.; Juaristi, J. I. Surface electron density models for accurate ab initio molecular dynamics with electronic friction. *Physical Review B* **2016**, *93*.

(24) Palummo, M.; Bernardi, M.; Grossman, J. C. Exciton Radiative Lifetimes in Two-Dimensional Transition Metal Dichalcogenides. *Nano Letters* **2015**, *15*, 2794–2800.

(25) Bai, R.; Guo, P.; Yu, S.; Cai, Z.; Chen, S.; Wu, Y.-N. Excited-State Carrier Dynamics in Knock-on Damage of Monolayer MoS<sub>2</sub> from First Principles. *The Journal of Physical Chemistry Letters* **2025**, *16*, 3809–3815.

(26) Shi, H.; Yan, R.; Bertolazzi, S.; Brivio, J.; Gao, B.; Kis, A.; Jena, D.; Xing, H. G.; Huang, L. Exciton Dynamics in Suspended Monolayer and Few-Layer MoS<sub>2</sub> 2D Crystals. *ACS Nano* **2013**, *7*, 1072–1080.

(27) Kozubek, R.; Tripathi, M.; Ghorbani-Asl, M.; Kretschmer, S.; Madauß, L.; Pollmann, E.; O'Brien, M.; McEvoy, N.; Ludacka, U.; Susi, T.; Duesberg, G. S.; Wilhelm, R. A.; Krasheninnikov, A. V.; Kotakoski, J.; Schleberger, M. Perforating Free-standing Molybdenum Disulfide Monolayers with Highly Charged Ions. *The Journal of Physical Chemistry Letters* **2019**, *10*, 904–910.

(28) Grossek, A. S.; Niggas, A.; Wilhelm, R. A.; Aumayr, F.; Lemell, C. Model for Nanopore Formation in Two-Dimensional Materials by Impact of Highly Charged Ions. *Nano Letters* **2022**, *22*, 9679–9684.

(29) Niggas, A. et al. Ion-Induced Surface Charge Dynamics in Freestanding Monolayers of Graphene and MoS<sub>2</sub> Probed by the Emission of Electrons. *Physical Review Letters* **2022**, *129*.

(30) Skopinski, L.; Kretschmer, S.; Ernst, P.; Herder, M.; Madauß, L.; Breuer, L.; Krasheninnikov, A. V.; Schleberger, M. Velocity distributions of particles sputtered from supported two-dimensional MoS<sub>2</sub> during highly charged ion irradiation. *Physical Review B* **2023**, *107*.

(31) Masuda, S.; Harada, Y. Deexcitation of rare-gas metastable atoms on semiconductor surfaces: MoS<sub>2</sub> and LaCoO<sub>3</sub>. *Surface Science* **1993**, *283*, 78–83.

(32) Buitrago, P. F.; Romero, M. A.; Bonin, C. J.; Irusta, Y.; González, C.; Vidal, R.; García, E. A.; Bonetto, F. Neutralization of low-energy Ne+ colliding with MoS<sub>2</sub> and metallic molybdenum: An experimental and theoretical study. *Physical Review A* **2024**, *110*.

(33) Gainullin, I. K. Resonant charge transfer during ion scattering on metallic surfaces. *Physics-Uspekhi* **2020**, *63*, 888–906.

(34) Ghaderzadeh, S.; Ladygin, V.; Ghorbani-Asl, M.; Hlawacek, G.; Schleberger, M.; Krasheninnikov, A. V. Freestanding and Supported MoS<sub>2</sub> Monolayers under Cluster Irradiation: Insights from Molecular Dynamics Simulations. *ACS Applied Materials' Interfaces* **2020**, *12*, 37454–37463.

(35) Kretschmer, S.; Maslov, M.; Ghaderzadeh, S.; Ghorbani-Asl, M.; Hlawacek, G.; Krasheninnikov, A. V. Supported Two-Dimensional Materials under Ion Irradiation: The Substrate Governs Defect Production. *ACS Applied Materials' Interfaces* **2018**, *10*, 30827–30836.

(36) Wu, X.; Zhu, X.; Lei, B. Impact of ion beam irradiation on two-dimensional MoS<sub>2</sub>: a molecular dynamics simulation study. *Journal of Physics: Condensed Matter* **2021**, *34*, 055402.

(37) Bertolazzi, S.; Brivio, J.; Kis, A. Stretching and Breaking of Ultrathin MoS<sub>2</sub>. *ACS Nano* **2011**, *5*, 9703–9709.

(38) Albaridy, R.; Periyaganounder, D.; Naphade, D.; Lee, C.-J.; Hedhili, M.; Wan, Y.; Chang, W.-H.; Anthopoulos, T. D.; Tung, V.; Aljarb, A.; Schwingenschlögl, U. Strain-Induced Sulfur Vacancies in Monolayer MoS<sub>2</sub>. *ACS Materials Letters* **2023**, *5*, 2584–2593.

(39) Frisenda, R.; Drüppel, M.; Schmidt, R.; Michaelis de Vasconcellos, S.; Perez de Lara, D.; Bratschitsch, R.; Rohlfing, M.; Castellanos-Gomez, A. Biaxial strain tuning of the

optical properties of single-layer transition metal dichalcogenides. *npj 2D Materials and Applications* **2017**, *1*.

(40) Wang, W.; Yang, C.; Bai, L.; Li, M.; Li, W. First-Principles Study on the Structural and Electronic Properties of Monolayer MoS<sub>2</sub> with S-Vacancy under Uniaxial Tensile Strain. *Nanomaterials* **2018**, *8*, 74.

(41) Chopra, N. S.; Romadanov, I.; Raitses, Y. Production of warm ions in electron beam generated E × B plasma. *Applied Physics Letters* **2024**, *124*.

(42) Son, S. H.; Romadanov, I.; Chopra, N. S.; Raitses, Y. Planar laser-induced fluorescence system for spatiotemporal ion velocity distribution function measurements. *Plasma Sources Science and Technology* **2025**, *34*, 105003.

(43) Kretschmer, S.; Lehnert, T.; Kaiser, U.; Krasheninnikov, A. V. Formation of defects in two-dimensional MoS<sub>2</sub> in the transmission electron microscope at electron energies below the knock-on threshold: The role of electronic excitations. *Nano Lett.* **2020**, *20*, 2865–2870.

(44) Jones, L. A. H.; Xing, Z.; Swallow, J. E. N.; Shiel, H.; Featherstone, T. J.; Smiles, M. J.; Fleck, N.; Thakur, P. K.; Lee, T.-L.; Hardwick, L. J.; Scanlon, D. O.; Regoutz, A.; Veal, T. D.; Dhanak, V. R. Band Alignments, Electronic Structure, and Core-Level Spectra of Bulk Molybdenum Dichalcogenides (MoS<sub>2</sub>, MoSe<sub>2</sub>, and MoTe<sub>2</sub>). *The Journal of Physical Chemistry C* **2022**, *126*, 21022–21033.

(45) Ramana Murty, M.; Atwater, H. A. Low energy ion irradiation of H-terminated Si(001): hydrogen sputtering, beam-induced (2 × 1) reconstruction, and Si epitaxy. *Nuclear Instruments and Methods in Physics Research Section B: Beam Interactions with Materials and Atoms* **1995**, *102*, 293–300.

(46) Xie, J.; Zhang, J.; Li, S.; Grote, F.; Zhang, X.; Zhang, H.; Wang, R.; Lei, Y.; Pan, B.; Xie, Y. Controllable Disorder Engineering in Oxygen-Incorporated MoS<sub>2</sub> Ultrathin

Nanosheets for Efficient Hydrogen Evolution. *Journal of the American Chemical Society* **2013**, *135*, 17881–17888.

(47) Nan, H.; Wang, Z.; Wang, W.; Liang, Z.; Lu, Y.; Chen, Q.; He, D.; Tan, P.; Miao, F.; Wang, X.; Wang, J.; Ni, Z. Strong Photoluminescence Enhancement of MoS<sub>2</sub> through Defect Engineering and Oxygen Bonding. *ACS Nano* **2014**, *8*, 5738–5745.

(48) Kang, N.; Paudel, H. P.; Leuenberger, M. N.; Tetard, L.; Khondaker, S. I. Photoluminescence Quenching in Single-Layer MoS<sub>2</sub> via Oxygen Plasma Treatment. *The Journal of Physical Chemistry C* **2014**, *118*, 21258–21263.

(49) Chow, W. L.; Luo, X.; Quek, S. Q.; Tay, B. K. Evolution of Raman Scattering and Electronic Structure of Ultrathin Molybdenum Disulfide by Oxygen Chemisorption. *Advanced Electronic Materials* **2015**, *1*.

(50) Yang, J.; Kim, S.; Choi, W.; Park, S. H.; Jung, Y.; Cho, M.-H.; Kim, H. Improved Growth Behavior of Atomic-Layer-Deposited High-k Dielectrics on Multilayer MoS<sub>2</sub> by Oxygen Plasma Pretreatment. *ACS Applied Materials' Interfaces* **2013**, *5*, 4739–4744.

(51) Islam, M. R.; Kang, N.; Bhanu, U.; Paudel, H. P.; Erementchouk, M.; Tetard, L.; Leuenberger, M. N.; Khondaker, S. I. Tuning the electrical property via defect engineering of single layer MoS<sub>2</sub> by oxygen plasma. *Nanoscale* **2014**, *6*, 10033–10039.

(52) Yang, W.; Sun, Q.-Q.; Geng, Y.; Chen, L.; Zhou, P.; Ding, S.-J.; Zhang, D. W. The Integration of Sub-10 nm Gate Oxide on MoS<sub>2</sub> with Ultra Low Leakage and Enhanced Mobility. *Scientific Reports* **2015**, *5*.

(53) KC, S.; Longo, R. C.; Wallace, R. M.; Cho, K. Surface oxidation energetics and kinetics on MoS<sub>2</sub> monolayer. *Journal of Applied Physics* **2015**, *117*.

(54) Zhou, H.; Yu, F.; Liu, Y.; Zou, X.; Cong, C.; Qiu, C.; Yu, T.; Yan, Z.; Shen, X.;

Sun, L.; Yakobson, B. I.; Tour, J. M. Thickness-dependent patterning of MoS<sub>2</sub> sheets with well-oriented triangular pits by heating in air. *Nano Research* **2013**, *6*, 703–711.

(55) Pető, J.; Ollár, T.; Vancsó, P.; Popov, Z. I.; Magda, G. Z.; Dobrik, G.; Hwang, C.; Sorokin, P. B.; Tapasztó, L. Spontaneous doping of the basal plane of MoS<sub>2</sub> single layers through oxygen substitution under ambient conditions. *Nature Chemistry* **2018**, *10*, 1246–1251.

(56) Giannazzo, F.; Fisichella, G.; Greco, G.; Di Franco, S.; Deretzis, I.; La Magna, A.; Bongiorno, C.; Nicotra, G.; Spinella, C.; Scopelliti, M.; Pignataro, B.; Agnello, S.; Roccaforte, F. Ambipolar MoS<sub>2</sub> Transistors by Nanoscale Tailoring of Schottky Barrier Using Oxygen Plasma Functionalization. *ACS Applied Materials' Interfaces* **2017**, *9*, 23164–23174.

(57) Reidy, K.; Mortelmans, W.; Jo, S. S.; Penn, A. N.; Foucher, A. C.; Liu, Z.; Cai, T.; Wang, B.; Ross, F. M.; Jaramillo, R. Atomic-Scale Mechanisms of MoS<sub>2</sub>Oxidation for Kinetic Control of MoS<sub>2</sub>/MoO<sub>3</sub>Interfaces. *Nano Letters* **2023**, *23*, 5894–5901.

(58) Supplementary Information.

(59) Farigliano, L. M.; Paredes-Olivera, P. A.; Patrito, E. M. Ab-initio molecular dynamics simulations of the reactivity of MoS<sub>2</sub> towards F<sub>2</sub> molecules: Implications for etching processes. *Applied Surface Science* **2023**, *607*, 154637.

(60) Lee, B. J.; Lee, B. J.; Efremov, A.; Yang, J.-W.; Kwon, K.-H. Etching Characteristics and Mechanisms of MoS<sub>2</sub> 2D Crystals in O<sub>2</sub>/Ar Inductively Coupled Plasma. *Journal of Nanoscience and Nanotechnology* **2016**, *16*, 11201–11209.

(61) Woodworth, J. R.; Riley, M. E.; Meister, D. C.; Aragon, B. P.; Le, M. S.; Sawin, H. H. Ion energy and angular distributions in inductively coupled radio frequency discharges in argon. *Journal of Applied Physics* **1996**, *80*, 1304–1311.

(62) Yan, H.; Chen, H.; Cui, X.; Guan, Q.; Wang, B.; Cai, Y. Unraveling energetics and states of adsorbing oxygen species with MoS<sub>2</sub> for modulated work function. *Nanoscale Horizons* **2025**, *10*, 359–368.

(63) O’Neil, M. J. *The Merck Index — An Encyclopedia of Chemicals, Drugs, and Biologicals (Merck Index)*; Merck, 2006.

(64) Kühne, T. D. et al. CP2K: An electronic structure and molecular dynamics software package - Quickstep: Efficient and accurate electronic structure calculations. *The Journal of Chemical Physics* **2020**, *152*.

(65) Hartwigsen, C.; Goedecker, S.; Hutter, J. Relativistic separable dual-space Gaussian pseudopotentials from H to Rn. *Physical Review B* **1998**, *58*, 3641–3662.

(66) Frigo, M.; Johnson, S. The Design and Implementation of FFTW3. *Proceedings of the IEEE* **2005**, *93*, 216–231.

(67) Krack, M. Pseudopotentials for H to Kr optimized for gradient-corrected exchange-correlation functionals. *Theoretical Chemistry Accounts* **2005**, *114*, 145–152.

(68) VandeVondele, J.; Hutter, J. Gaussian basis sets for accurate calculations on molecular systems in gas and condensed phases. *The Journal of Chemical Physics* **2007**, *127*.

(69) Grimme, S.; Ehrlich, S.; Goerigk, L. Effect of the damping function in dispersion corrected density functional theory. *Journal of Computational Chemistry* **2011**, *32*, 1456–1465.

(70) Borštník, U.; VandeVondele, J.; Weber, V.; Hutter, J. Sparse matrix multiplication: The distributed block-compressed sparse row library. *Parallel Computing* **2014**, *40*, 47–58.

(71) Heinecke, A.; Henry, G.; Hutchinson, M.; Pabst, H. LIBXSMM: Accelerating Small Matrix Multiplications by Runtime Code Generation. **2016**, 981–991.

(72) Schütt, O.; Messmer, P.; Hutter, J.; VandeVondele, J. GPU-Accelerated Sparse Matrix–Matrix Multiplication for Linear Scaling Density Functional Theory. *Electronic Structure Calculations on Graphics Processing Units* **2016**, 173–190.

(73) Goerigk, L.; Hansen, A.; Bauer, C.; Ehrlich, S.; Najibi, A.; Grimme, S. A look at the density functional theory zoo with the advanced GMTKN55 database for general main group thermochemistry, kinetics and noncovalent interactions. *Physical Chemistry Chemical Physics* **2017**, *19*, 32184–32215.

(74) Farmilo, A.; Wilkinson, F. On the mechanism of quenching of singlet oxygen in solution. *Photochemistry and Photobiology* **1973**, *18*, 447–450.

(75) Petrov, E. G.; Robert, B.; Lin, S. H.; Valkunas, L. Theory of Triplet Excitation Transfer in the Donor-Oxygen-Acceptor System: Application to Cytochrome b 6 f. *Biophysical Journal* **2015**, *109*, 1735–1745.

(76) Dagdigian, P. J.; Alexander, M. H.; Kłos, J. Theoretical investigation of the dynamics of O(1D→3P) electronic quenching by collision with Xe. *The Journal of Chemical Physics* **2015**, *143*.

(77) Famá, M.; Shi, J.; Baragiola, R. Sputtering of ice by low-energy ions. *Surface Science* **2008**, *602*, 156–161.

(78) Hagstrum, H. D. Auger Electron Ejection from Germanium and Silicon by Noble Gas Ions. *Physical Review* **1960**, *119*, 940–952.

(79) Goedecker, S.; Teter, M.; Hutter, J. Separable dual-space Gaussian pseudopotentials. *Physical Review B* **1996**, *54*, 1703–1710.

(80) Hutter, J.; Iannuzzi, M.; Schiffmann, F.; VandeVondele, J. cp2k: atomistic simulations of condensed matter systems. *WIREs Computational Molecular Science* **2013**, *4*, 15–25.

(81) VandeVondele, J.; Krack, M.; Mohamed, F.; Parrinello, M.; Chassaing, T.; Hutter, J. Quickstep: Fast and accurate density functional calculations using a mixed Gaussian and plane waves approach. *Computer Physics Communications* **2005**, *167*, 103–128.

(82) Lippert, G.; Hutter, J.; Parrinello, M. A hybrid Gaussian and plane wave density functional scheme. *Molecular Physics* **1997**, *92*, 477–487.

(83) VandeVondele, J.; Hutter, J. An efficient orbital transformation method for electronic structure calculations. *The Journal of Chemical Physics* **2003**, *118*, 4365–4369.

(84) Kühne, T. D.; Krack, M.; Mohamed, F. R.; Parrinello, M. Efficient and Accurate Car-Parrinello-like Approach to Born-Oppenheimer Molecular Dynamics. *Physical Review Letters* **2007**, *98*.

(85) Kolafa, J. Time-reversible always stable predictor–corrector method for molecular dynamics of polarizable molecules. *Journal of Computational Chemistry* **2003**, *25*, 335–342.

(86) Weber, V.; VandeVondele, J.; Hutter, J.; Niklasson, A. M. N. Direct energy functional minimization under orthogonality constraints. *The Journal of Chemical Physics* **2008**, *128*.

(87) Hamilton, T. P.; Pulay, P. Direct inversion in the iterative subspace (DIIS) optimization of open-shell, excited-state, and small multiconfiguration SCF wave functions. *The Journal of Chemical Physics* **1986**, *84*, 5728–5734.

(88) Perdew, J. P.; Burke, K.; Ernzerhof, M. Generalized Gradient Approximation Made Simple. *Physical Review Letters* **1996**, *77*, 3865–3868.

(89) Furness, J. W.; Kaplan, A. D.; Ning, J.; Perdew, J. P.; Sun, J. Accurate and Numerically Efficient r2SCAN Meta-Generalized Gradient Approximation. *The Journal of Physical Chemistry Letters* **2020**, *11*, 8208–8215.

(90) Sabatini, R.; Gorni, T.; de Gironcoli, S. Nonlocal van der Waals density functional made simple and efficient. *Physical Review B* **2013**, *87*.

(91) Grimme, S.; Antony, J.; Ehrlich, S.; Krieg, H. A consistent and accurateab initioparametrization of density functional dispersion correction (DFT-D) for the 94 elements H-Pu. *The Journal of Chemical Physics* **2010**, *132*.

(92) Ning, J.; Kothakonda, M.; Furness, J. W.; Kaplan, A. D.; Ehlert, S.; Brandenburg, J. G.; Perdew, J. P.; Sun, J. Workhorse minimally empirical dispersion-corrected density functional with tests for weakly bound systems: r2SCAN + rVV10. *Physical Review B* **2022**, *106*.

(93) consortium, T. P. Promoting transparency and reproducibility in enhanced molecular simulations. *Nature Methods* **2019**, *16*, 670–673.

(94) Tribello, G. A.; Bonomi, M.; Branduardi, D.; Camilloni, C.; Bussi, G. PLUMED 2: New feathers for an old bird. *Computer Physics Communications* **2014**, *185*, 604–613.

(95) Bonomi, M.; Branduardi, D.; Bussi, G.; Camilloni, C.; Provati, D.; Raiteri, P.; Donadio, D.; Marinelli, F.; Pietrucci, F.; Broglia, R. A.; Parrinello, M. PLUMED: A portable plugin for free-energy calculations with molecular dynamics. *Computer Physics Communications* **2009**, *180*, 1961–1972.

(96) Barducci, A.; Bussi, G.; Parrinello, M. Well-Tempered Metadynamics: A Smoothly Converging and Tunable Free-Energy Method. *Physical Review Letters* **2008**, *100*.

(97) Laio, A.; Parrinello, M. Escaping free-energy minima. *Proceedings of the National Academy of Sciences* **2002**, *99*, 12562–12566.

(98) Peng, H.; Perdew, J. P. Rehabilitation of the Perdew-Burke-Ernzerhof generalized gradient approximation for layered materials. *Physical Review B* **2017**, *95*.

(99) Young, P. A. Lattice parameter measurements on molybdenum disulphide. *Journal of Physics D: Applied Physics* **1968**, *1*, 936–938.